

CZECH TECHNICAL UNIVERSITY IN PRAGUE,
FACULTY OF ELECTRICAL ENGINEERING

MASTER'S THESIS

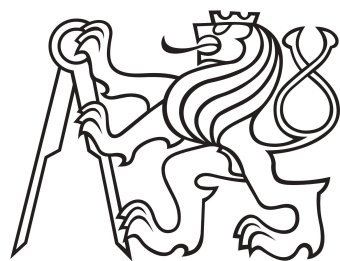
Dual Circularly Polarized Waveguide Antenna

Author

M. ŠIMÁK
DEPARTMENT OF
ELECTROMAGNETIC FIELD

Supervisor

doc. Ing. P. HAZDRA, Ph.D.
DEPARTMENT OF
ELECTROMAGNETIC FIELD



January 2025

I. Personal and study details

Student's name: **Šimák Martin** Personal ID number: **483523**
Faculty / Institute: **Faculty of Electrical Engineering**
Department / Institute: **Department of Electromagnetic Field**
Study program: **Electronics and Communications**
Specialisation: **Radio Communications and Systems**

II. Master's thesis details

Master's thesis title in English:

Dual Circularly Polarized Waveguide Antenna

Master's thesis title in Czech:

Duálně kruhově polarizovaná vlnovodová anténa

Guidelines:

Research different polarizers in a metallic waveguide, consider round or square transversal shape of the guide. Inspired by circularly polarized patch antenna with chamfered corners, adapt this technique to the waveguide technology (the frequency should be used to be appropriate for easy fabrication, say around 5 GHz). Perform 2D eigenmode analysis of round and square waveguides with inserted metal triangles, and compare the results with the theory of patch antennas of such shapes. Choose one of the waveguide with the polarizer and optimize it to provide the best bandwidth and radiation properties, also design the transition from coaxial cable, preferably with the ability to excite both RHCP and LHCP patterns. Add a small horn (say 15 dBi) to the waveguide and finally optimise the whole structure. Build and measure the whole structure, compare to simulation results.

Bibliography / sources:

- 1/ Polarizers on sections of square waveguides with inner corner ridges | IEEE Conference Publication | IEEE Xplore
- 2/ Compact reconfigurable waveguide circular polarizer | IEEE Conference Publication | IEEE Xplore
- 3/ Design of Wideband Quad-Ridge Waveguide Polarizer | IEEE Conference Publication | IEEE Xplore
- 4/ Optimum-Iris-Set Concept for Waveguide Polarizers | IEEE Journals & Magazine | IEEE Xplore
- 5/ Novel square/rectangle waveguide septum polarizer | IEEE Conference Publication | IEEE Xplore
- 6/ Broadband Septum Polarizer With Triangular Common Port | IEEE Journals & Magazine | IEEE Xplore
- 7/ New Tunable Iris-Post Square Waveguide Polarizers for Satellite Information Systems | IEEE Conference Publication | IEEE Xplore
- 8/ Hexagonal waveguides: New class of waveguides for mm-wave circularly polarized horns | IEEE Conference Publication | IEEE Xplore
- 9/ Hexagonal Waveguide Based Circularly Polarized Horn Antennas for Sub-mm-Wave/Terahertz Band | IEEE Journals & Magazine | IEEE Xplore
- Bow-Tie-Shaped Radiating Element for Single and Dual Circular 10/ Polarization | IEEE Journals & Magazine | IEEE Xplore
- 11/ A Wideband Circularly Polarized Horn Antenna With a Tapered Elliptical Waveguide Polarizer | IEEE Journals & Magazine | IEEE Xplore

Name and workplace of master's thesis supervisor:

doc. Ing. Pavel Hazdra, Ph.D. FEE CTU in Prague, K 13117

Name and workplace of second master's thesis supervisor or consultant:

Date of master's thesis assignment: **04.09.2024**

Deadline for master's thesis submission: _____

Assignment valid until: **15.02.2026**

doc. Ing. Pavel Hazdra, Ph.D.
Supervisor's signature

Head of department's signature

prof., Mgr. Petr Páta, Ph.D.
Dean's signature

III. Assignment receipt

The student acknowledges that the master's thesis is an individual work. The student must produce his thesis without the assistance of others, with the exception of provided consultations. Within the master's thesis, the author must state the names of consultants and include a list of references.

Date of assignment receipt

Student's signature

Declaration

I declare that I completed the presented thesis independently and that all used sources are quoted in accordance with the Methodological instructions that cover the ethical principles for writing an academic thesis.

Prohlášení

Prohlašuji, že jsem předloženou práci vypracoval samostatně a že jsem uvedl veškeré použité informační zdroje v souladu s Metodickým pokynem o dodržování etických principů při přípravě vysokoškolských závěrečných prací.

V Praze -----

Martin Šimák

Acknowledgements

First and foremost, I would like to express my gratitude to my supervisor, Pavel Hazdra, for his professional help, willingness, and reliable correspondence throughout our collaboration, which was conducted remotely during my double degree program in cooperation with the National Taiwan University of Science and Technology. I would also like to thank professor Ding-Bing Lin, my supervisor at the partner university, for his initiative and valuable assistance, especially in the design production.

Last but not least, I would like to thank all my loved ones who supported me from afar throughout my studies, especially my family and friends. Special thanks go to Ester Jančáříková for standing by me and helping me through difficult times.

Poděkování

Především bych rád poděkoval svému vedoucímu, Pavlu Hazdrovi, za jeho odbornou pomoc, vstřícnost, a ochotu v podobě spolehlivé korespondence během spolupráce, která probíhala distančně v rámci mého studia double degree programu ve spolupráci s National Taiwan University of Science and Technology. Dále děkuji profesoru Ding-Bing Linovi, svému vedoucímu na partnerské univerzitě, za jeho iniciativu a cennou pomoc, zejména při výrobě návrhu.

V neposlední řadě bych rád poděkoval všem svým blízkým, kteří mě na dálku podporovali během celého studia, zejména své rodině a přátelům. Zvláštní poděkování na závěr potom patří Ester Jančáříkové za to, že stála při mě a byla mi oporou v nelehkých chvílích.

Title:

Dual Circularly Polarized Waveguide Antenna

Author: Martin Šimák

Study programme: Electronics and Communications

Supervisor: doc. Ing. Pavel Hazdra, Ph.D., Department of Electromagnetic Field FEE

Abstract:

This thesis details the design, simulation, fabrication, and measurement of a novel dual circularly polarized antenna operating in the 4.7 GHz to 5.7 GHz band. The system comprises a square waveguide polarizer with chamfered corners, a dual-coaxial feed, and a conical horn antenna. The polarizer generates right-hand and left-hand circular polarization by selectively exciting one of the two fundamental modes of the square waveguide. The dual coaxial feed provides the necessary excitation. The conical horn, designed using Antenna Magus and adapted to the polarizer, achieves a target gain of 15 dBi. CST Studio Suite was used for electromagnetic simulations, while Python with SciPy enabled dynamic optimization for enforcing geometric constraints. The fabricated antenna's measured performance closely aligns with simulations, demonstrating an axial ratio below 5 dB across the band and a measured gain of approximately 18 dBi at the centre frequency. This work contributes to a compact, manufacturable, dual circularly polarized antenna design with potential applications in satellite communications, radar, and other wireless systems.

Keywords: circular polarization, waveguide polarizer, dual-feed, conical horn antenna, hexagonal waveguide, eigenmode analysis, electromagnetic simulation

Název práce:

Duálně kruhově polarizovaná vlnovodová anténa

Autor: Martin Šimák

Studijní program: Elektronika a komunikace

Vedoucí: doc. Ing. Pavel Hazdra, Ph.D., Katedra elektromagnetického pole FEL

Abstrakt:

Tato diplomová práce popisuje návrh, simulaci, výrobu a měření duální kruhově polarizované antény pracující v pásmu 4.7 GHz až 5.7 GHz. Systém se skládá ze čtvercového vlnovodného polarizátoru se zkosenými rohy, dvojitého koaxiálního napájení a kuželové antény. Polarizátor generuje pravotočivou a levotočivou kruhovou polarizaci selektivně buzené jedním ze dvou základních módů čtvercového vlnovodu. Potřebné buzení zajistuje duální koaxiální napájení. Kuželová anténa navržená pomocí programu Antenna Magus a přizpůsobená polarizátoru dosahuje cílového zisku 15 dBi. Pro elektromagnetické simulace byla použit software CST Studio Suite, zatímco Python s použitím knihovny SciPy umožnil dynamickou optimalizaci pro vynucení geometrických omezení. Naměřený výkon zhotovené antény se přesně shoduje se simulacemi a vykazuje osový poměr pod 5 dBi v celém pásmu a naměřený zisk přibližně 18 dBi na střední frekvenci. Tato práce přináší kompaktní, výrobiteľnou konstrukci duální kruhově polarizované antény s potenciálním využitím v satelitní komunikaci, radarové technice a dalších bezdrátových systémech.

Klíčová slova: kruhová polarizace, vlnovodový polarizátor, duální napájení, kuželová anténa, hexagonální vlnovod, analýza vlastních módů, elektromagnetická simulace

Contents

Introduction	5
1 Electrodynamics of guided waves	7
1.1 Fundamentals of electrodynamics	7
1.1.1 Maxwell's equations	7
1.1.2 Electromagnetic properties of matter	8
1.1.3 Boundary conditions	10
1.2 Electromagnetic waves	10
1.2.1 The wave equations	10
1.2.2 Monochromatic plane waves	11
1.2.3 Polarization	14
1.2.4 Guided waves	16
2 Polarizer	20
2.1 Principle of operation	20
2.2 Literature survey	21
2.3 Eigenmode analysis	23
2.3.1 Figures of merit	25
2.3.2 Comparison of symmetric waveguides	26
2.4 Square waveguide polarizer	29
2.4.1 Simulation results	30
3 Feeding structure	32
3.1 Coaxial-to-waveguide transition	32
3.2 Dual feed	35
3.2.1 Grating	36
3.2.2 Second feed	37
4 Antenna	40
4.1 Conical horn	40

5 Final structure	43
5.1 Feed rework	43
5.2 Product finalization	45
Conclusion	49
A Constrained optimization	51
B Measurement results	56
Bibliography	63

List of Figures

2.1	Symmetric polarizers: models	23
2.2	Symmetric waveguides: fundamental modes	24
2.3	Symmetric polarizers: fundamental modes	24
2.4	Polarizers: cutoff frequencies	27
2.5	Square polarizer: cross-section tuning	28
2.6	Circular polarizer: cross-section tuning	28
2.7	Final polarizer: model	30
2.8	Final polarizer: radiation properties	31
3.1	Single feed: section views	33
3.2	Single feed: reflection	34
3.3	Dual feed: section views	35
3.4	Single feed with grating: grating distance sweep	36
3.5	Cavity resonance: electric field section views	37
3.6	Single feed with grating: reflection	37
3.7	Dual feed: S-parameters	38
3.8	Final dual feed: model	39
4.1	Conical horn: models	41
4.2	Conical horn: performance	42
5.1	Final structure: grating performance	44
5.2	Final structure: MVP model	44
5.3	Final structure: DFM model	45
5.4	Measurement results: S-parameters	46
5.5	Measurement results: gain and aperture efficiency	46
5.6	Measurement results: axial ratio	47
5.7	Back view of the final structure	48
B.1	Measurement setup	56
B.2	Measurement 1: S-parameters	57

B.3	Measurement 1: gain and axial ratio	57
B.4	Measurement 1: elevation radiation pattern ($\varphi = 90^\circ$)	58
B.5	Measurement 1: azimuth radiation pattern ($\varphi = 0^\circ$)	59
B.6	Measurement 2: S-parameters	60
B.7	Measurement 2: gain and axial ratio	60
B.8	Measurement 2: elevation radiation pattern ($\varphi = 90^\circ$)	61
B.9	Measurement 2: azimuth radiation pattern ($\varphi = 0^\circ$)	62

Introduction

This thesis focuses on the design and implementation of a dual circularly polarized antenna operating within the 4.7 GHz to 5.7 GHz frequency band. This range, a subset of the C-band, finds widespread use in various applications such as satellite communications, radar systems, and certain Wi-Fi standards. The selection of this frequency band was driven by the increasing demand for high-bandwidth, reliable communication and the availability of established waveguide technology within this range.

The design process leveraged several software tools. CST Studio Suite [1] was the primary tool for full-wave electromagnetic simulations due to its comprehensive features for modelling and simulating complex electromagnetic structures, including waveguides and antennas. Its transient solver, based on the Finite Integration Technique (FIT), was particularly suitable for analysing the time-domain behaviour of the proposed designs. Antenna Magus [2] was integrated into the initial design stages, specifically for the conical horn antenna, expediting the prototyping process through its extensive database of antenna designs and ability to synthesize antenna geometries based on user-defined parameters. Advanced optimization routines were implemented in Python using the SciPy library [3]. SciPy, an open-source library built upon NumPy, offers a wide range of numerical algorithms, including those used to implement constrained optimization, as detailed in Appendix A. The Nelder-Mead method, a derivative-free optimization technique, was employed to optimize the geometric parameters of the polarizer and the feeding structure. This method is well-suited for problems with non-smooth or noisy objective functions, which can arise from complex electromagnetic simulations. It was utilized both within CST's native optimizer tool and within the Python-based SciPy optimization framework. MATLAB [4] was employed for data visualization and generating publication-ready plots due to its robust plotting capabilities and fine-grained control over figure aesthetics.

Synopsis. **Chapter 1** establishes the theoretical foundations of electromagnetic wave propagation in guided structures, starting from Maxwell's equations and culminating in the derivation of the wave equations for waveguide modes.

Chapter 2 details the design and analysis of the waveguide polarizer, exploring various polarizer designs, and ultimately focusing on a novel approach utilizing a square waveguide with chamfered corners.

Chapter 3 addresses the challenge of efficiently exciting the two orthogonal modes within the square waveguide using a dual-coaxial feed. A modified feeding structure is presented and optimized for minimal reflection and cross-talk.

Chapter 4 focuses on the design of a conical horn antenna, specifically adapted to interface with the square waveguide output of the polarizer developed in Chapter 2. This section discusses the optimization of the horn's geometry for achieving the desired gain and radiation characteristics.

Chapter 5 details the culmination of the design process, integrating the individual components developed in previous chapters into a complete antenna system, and outlines the final design adjustments. Furthermore, it presents a comprehensive comparison of the simulated and measured performance results of the fabricated prototype, including a thorough discussion of the observed agreement and discrepancies.

Methodology. The methodology combined numerical simulations with experimental validation. Full-wave electromagnetic simulations, conducted using CST Studio Suite, were used to analyse the performance of individual components and the integrated antenna system. Optimization algorithms, implemented in both CST Studio Suite and Python using the SciPy library, refined the design parameters for optimal performance. A prototype of the finalized design was fabricated and measured to validate the simulation results and demonstrate the feasibility of the proposed approach.

Chapter 1

Electrodynamics of guided waves

This chapter establishes the theoretical foundation for the analysis and design of a waveguide-based antenna system. Beginning with Maxwell's equations and a general description of electromagnetic fields in various settings relevant to this work, the wave equations governing guided waves are derived, and their solutions are analysed to elucidate the behaviour of electromagnetic fields within waveguides. This analysis provides a framework for understanding the operation of structures designed in the following chapters. While focusing on the essential elements of waveguide theory, this chapter provides a comprehensive treatment of the subject and establishes the notation used throughout this work.

The exposition endeavours to take inspiration and build upon the foundations laid in [5]–[7], incorporating personal insights and notational preferences to present a cohesive theoretical framework for further chapters.

1.1 Fundamentals of electrodynamics

This section presents the fundamental principles of electromagnetism, starting with Maxwell's equations, which encapsulate the relationships between electric and magnetic fields and their sources. The response of different materials to these fields is then explored through the introduction of *constitutive relations*. Finally, the focus is shifted to the behaviour of electromagnetic fields at material boundaries, providing essential *boundary conditions* for solving electromagnetic problems.

1.1.1 Maxwell's equations

The differential form of Maxwell's equations, as presented below, constitutes the cornerstone of classical electromagnetism, providing a complete¹ framework for analysing electromagnetic phenomena at any point in space and time. These equations summarize the relations between *electric field* \mathbf{E} and *magnetic field* \mathbf{B} and their sources due to charge densities ρ , current densities \mathbf{J} , or the changing of the fields themselves. To ensure the validity of these expressions, let us assume that the field vectors are well-behaved functions exhibiting continuity and possessing continuous derivatives. This assumption holds for most electromagnetic systems, with exceptions arising at interfaces between distinct media where abrupt changes in charge and current densities may occur.

¹For actual completeness, save for some special properties stemming from interactions in matter, the equations must also be supplemented by the Lorentz's force law $\mathbf{F} = q(\mathbf{E} + \mathbf{v} \times \mathbf{B})$.

$$\nabla \cdot \mathbf{E} = \frac{1}{\epsilon_0} \rho_e, \quad (1.1a)$$

$$\nabla \times \mathbf{E} = -\mu_0 \mathbf{J}_m - \partial_t \mathbf{B}, \quad (1.1b)$$

$$\nabla \cdot \mathbf{B} = \mu_0 \rho_m, \quad (1.1c)$$

$$\nabla \times \mathbf{B} = \mu_0 \mathbf{J}_e + \mu_0 \epsilon_0 \partial_t \mathbf{E}, \quad (1.1d)$$

A notable aspect of equations (1.1) is the inclusion of the magnetic charge density ρ_m and magnetic current density \mathbf{J}_m , which are part of the “generalized concept”. Although these quantities, despite diligent search, were never physically observed, their introduction establishes a pleasing balance in Maxwell’s equations while being theoretically sound as well. This concept is further utilized when solving advanced physical problems in applied physics and engineering. This is facilitated by the introduction of equivalent magnetic charge and current, which can be used to conveniently express fields as if generated by these fictitious sources, especially in problems where the exact form of the electromagnetic field would otherwise be complicated to elucidate.

Mathematically, equations (1.1), like any differential equations, form a complete problem only when supplemented with suitable boundary conditions in a more traditional sense, such as the behaviour of the vector fields “in infinity”. These are typically “obvious” from the problem-solving context, e.g., fields vanishing at large distances from localized charge distribution, etc.

1.1.2 Electromagnetic properties of matter

Although Maxwell’s equations in their fundamental form (1.1) provide a complete description of electromagnetic phenomena, an alternative formulation offers a more convenient approach for analysing materials susceptible to electric and magnetic polarization.

Within such media, the total electric charge density ρ_e can be expressed as a sum of the *free charge* density ρ_f , which constitutes the *actual source* charge,² and the *bound charge* $\rho_b = -\nabla \cdot \mathbf{P}$, produced by an electric polarization \mathbf{P} of the material. Moreover, changing electric fields also induce changing polarization, producing *polarization current* $\mathbf{J}_p = \partial_t \mathbf{P}$, which adds to the *free current* \mathbf{J}_f . Similarly to electric polarization, a magnetic polarization \mathbf{M} results in a bound current $\mathbf{J}_b = \nabla \times \mathbf{M}$. These effects, inherently connected to the susceptibility of materials to be polarized, influence the total electromagnetic field in their vicinity. Consequently, auxiliary field quantities were introduced that account for the presence of such media

$$\mathbf{D} = \epsilon_0 (\mathbf{E} + \mathbf{P}), \quad (1.2a)$$

$$\mathbf{H} = \frac{1}{\mu_0} \mathbf{H} - \mathbf{M}. \quad (1.2b)$$

This approach allows for expressing Maxwell’s equations in a form that directly relates the electric and magnetic fields to the free charge and free current, which are sources that can be controlled directly. Using the field quantities defined by equations (1.2), Maxwell’s equations (1.1) read

$$\nabla \cdot \mathbf{D} = \rho_f, \quad (1.3a)$$

$$\nabla \times \mathbf{E} = -\mathbf{J}_m - \partial_t \mathbf{B}, \quad (1.3b)$$

$$\nabla \cdot \mathbf{B} = \rho_m, \quad (1.3c)$$

$$\nabla \times \mathbf{H} = \mathbf{J}_f + \partial_t \mathbf{D}, \quad (1.3d)$$

While equations (1.3) effectively express electromagnetic laws within media, their

²It is important to reinforce the idea that the magnetic charge and current are fictitious “source” quantities. Therefore, they are already, by definition, purely *free* quantities.

hybrid notation, involving both \mathbf{E} and \mathbf{D} and \mathbf{B} and \mathbf{H} , necessitates the use of *constitutive relations*. These relations, which establish correspondence between the respective electric and magnetic field quantities, are material-dependent and reflect the specific response of a medium to electric and magnetic fields. These relationships can generally be expressed as

$$\mathbf{D} = \hat{\epsilon} * \mathbf{E}, \quad (1.4a)$$

$$\mathbf{B} = \hat{\mu} * \mathbf{H}, \quad (1.4b)$$

where $\hat{\epsilon}$ and $\hat{\mu}$ are the material's *permittivity* and *permeability*, respectively, and the asterisk denotes *convolution*.

Remark 1.1.1. In formulations akin to equations (1.3), emphasizing the separation of free and bound sources, some authors also prefer to dissect the free current further. This current is generally conceptualized as the current "not directly tied to the bound charges" within a material. A few commonly recognized examples are *convection current*, *beam current*, and *conduction current*. In electrical engineering, it is the conduction current that arises from the movement of charges, typically electrons, that can move freely throughout the material. This kinetic energy of charges in conductors is the main cause of losses in waveguides and can be expressed by

$$\mathbf{J}_c = \hat{\sigma} * \mathbf{E}, \quad (1.5)$$

where $\hat{\sigma}$ is the material's *conductivity*. Equation (1.5), together with equations (1.4), completes the required set of constitutive relations.

The *constitutive parameters* $\hat{\epsilon}$, $\hat{\mu}$, and $\hat{\sigma}$, generally represented as complex second-rank tensors, establish the relationship between the applied electromagnetic fields and the material's response. The functional dependencies of these tensors provide a classification scheme for material properties:

- *Linearity:* A material is classified as linear if its constitutive parameters are independent of the applied field strength; otherwise, it is considered nonlinear.
- *Homogeneity:* If the constitutive parameters are invariant with respect to position within the material, it is deemed homogeneous; conversely, spatial dependence indicates an inhomogeneous medium.
- *Isotropy:* Materials exhibiting constitutive parameters independent of the applied field's direction are classified as isotropic. Conversely, direction-dependent parameters signify an anisotropic material, with crystals being a prime example.
- *Dispersion:* Materials whose constitutive parameters exhibit frequency dependence are categorized as dispersive. While some materials demonstrate negligible frequency dependence and can be effectively considered nondispersive, all materials encountered in practice exhibit some degree of dispersion.

Example 1.1.2 [Constitutive relations in free space]. In the simplest case of free space, equations (1.4a), (1.4b), and (1.5) become

$$\hat{\epsilon} = \epsilon_0 \approx 8.854 \times 10^{-12} \text{ F m}^{-1}, \quad (1.6a)$$

$$\hat{\mu} = \mu_0 = 4\pi \times 10^{-7} \text{ H m}^{-1}, \quad (1.6b)$$

$$\hat{\sigma} = \sigma_0 = 0 \text{ S m}^{-1}. \quad (1.6c)$$

1.1.3 Boundary conditions

While the differential form of Maxwell's equations is a powerful tool for analysing electromagnetic fields within continuous media, material boundaries introduce discontinuities that require special treatment. These discontinuities in the fields arise at interfaces between media with different electrical properties or at surfaces carrying charge or current densities. To accurately describe the behaviour of the fields across such boundaries, Maxwell's equations in their integral form, which naturally incorporate these discontinuities, are more convenient. This form is obtained by applying integral theorems from vector calculus to equations (1.3), which then take on the form of

$$\oint_S \mathbf{D} \cdot d\mathbf{a} = Q_e, \quad (1.7a)$$

$$\oint_{\partial S} \mathbf{E} \cdot dl = - \int_S \mathbf{J}_m \cdot d\mathbf{a} - \frac{d}{dt} \int_S \mathbf{B} \cdot d\mathbf{a}, \quad (1.7b)$$

$$\oint_S \mathbf{B} \cdot d\mathbf{a} = Q_m, \quad (1.7c)$$

$$\oint_{\partial S} \mathbf{H} \cdot dl = \int_S \mathbf{J}_e \cdot d\mathbf{a} + \frac{d}{dt} \int_S \mathbf{D} \cdot d\mathbf{a}, \quad (1.7d)$$

where S is any closed surface.

Consider a boundary between two different media. The first medium is characterized by permittivity ϵ_1 and permeability μ_1 , while the second medium is characterized by permittivity ϵ_2 and permeability μ_2 . At this interface, electric and magnetic surface charge densities may be present, denoted by q_f and q_m , respectively. Additionally, electric and magnetic surface current densities, denoted by j_f and j_m , respectively, may also exist. The general *boundary conditions* for electrodynamics are then obtained by applying equations (1.7) to arbitrary surfaces encompassing a portion of the interface, yielding

$$\mathbf{e}_n \cdot (\mathbf{D}_1 - \mathbf{D}_2) = q_f, \quad (1.8a)$$

$$-\mathbf{e}_n \times (\mathbf{E}_1 - \mathbf{E}_2) = j_m, \quad (1.8b)$$

$$\mathbf{e}_n \cdot (\mathbf{B}_1 - \mathbf{B}_2) = q_m, \quad (1.8c)$$

$$\mathbf{e}_n \times (\mathbf{H}_1 - \mathbf{H}_2) = j_f. \quad (1.8d)$$

1.2 Electromagnetic waves

With the foundations of electromagnetism established, the focus is now shifted to one of its most significant consequences: the existence of electromagnetic waves. In this section, the manner in which Maxwell's equations predict the propagation of these waves is explored. The wave equations for the electric and magnetic fields are derived, revealing their interconnected nature and ability to sustain each other even in the absence of sources. Subsequently, the simplest and most fundamental solutions to these equations, *monochromatic plane waves*, are investigated. Finally, the confinement and guidance of these plane waves within conducting cavities are examined, laying the groundwork for understanding waveguides and resonant structures.

1.2.1 The wave equations

Maxwell's equations provide a comprehensive description of electromagnetic phenomena, but their coupled nature can make them challenging to solve directly. Decoupling

the equations and expressing them individually in terms of the electric and magnetic fields is often advantageous to facilitate analysis, particularly in source-free regions. Inside regions with no *free* charge or *free* current, Maxwell's equations (1.3) take on the form of

$$\nabla \cdot \mathbf{D} = 0, \quad (1.9a)$$

$$\nabla \times \mathbf{E} = -\partial_t \mathbf{B}, \quad (1.9b)$$

$$\nabla \cdot \mathbf{B} = 0, \quad (1.9c)$$

$$\nabla \times \mathbf{H} = \sigma \mathbf{E} + \partial_t \mathbf{D}. \quad (1.9d)$$

Furthermore, if the medium is *linear* and *homogeneous*, Equation (1.9d) can be fully expressed in terms of \mathbf{E} . With this simplification, applying the curl to Equations (1.9b) and (1.9d) yields

$$\Delta \mathbf{E} = \mu\sigma \partial_t \mathbf{E} + \mu\epsilon \partial_t^2 \mathbf{E}, \quad (1.10a)$$

$$\Delta \mathbf{B} = \mu\sigma \partial_t \mathbf{B} + \mu\epsilon \partial_t^2 \mathbf{B}. \quad (1.10b)$$

Therefore, electric and magnetic fields in linear homogeneous media both clearly satisfy the wave equation with a linear damping term $\mu\sigma\partial_t$, introduced by conductive losses. Moreover, in regions with $\sigma = 0$, such as free space or ideal insulators, equations (1.10) simplify even more to

$$\Delta \mathbf{E} = \mu\epsilon \partial_t^2 \mathbf{E}, \quad (1.11a)$$

$$\Delta \mathbf{B} = \mu\epsilon \partial_t^2 \mathbf{B}, \quad (1.11b)$$

taking on the form of classical wave equations, which are ubiquitous in physics. This consequently yields the formula

$$v = \frac{1}{\sqrt{\epsilon\mu}} = \frac{c}{\sqrt{\epsilon_r\mu_r}} \quad (1.12)$$

for the speed of electromagnetic waves in linear homogeneous media.

Remark 1.2.1. Compared with the original Maxwell's equations (1.3), these equations form two systems of second-order partial differential equations but are now decoupled and provide an additional solving method for given boundary-value problems. However, it is important to note that the wave Equations (1.10a) and (1.10b) were derived from Maxwell's equations (1.9) by differentiation. This impedes their mathematical equivalence. More specifically, while every solution to Maxwell's equations must satisfy the wave equations, the converse is not true.

1.2.2 Monochromatic plane waves

The electromagnetic theory presented thus far describes general vector fields that vary in space and time. However, as shown in Section 1.2.1, electromagnetic fields in source-free regions exhibit wave behaviour. Nonetheless, these time-varying vector fields remain complex and challenging to analyse in practical systems. Consider the elementary solution to the wave equation

$$\hat{\psi}(\mathbf{r}, t) = \hat{\Psi}_0 \exp \left[i \left(\hat{\mathbf{k}} \cdot \mathbf{r} - \omega t \right) \right]. \quad (1.13)$$

Here, $\hat{\mathbf{k}}$ is the complex *wave vector* indicating the direction of wave propagation, and ω is the angular frequency of the wave. Equation (1.13) is expressed in terms of a *complex wave function* with a *complex amplitude* $\hat{\Psi}_0 \equiv \Psi_0 e^{i\delta}$. This quantity encapsulates both the *real amplitude* Φ_0 and the *phase shift* δ of the physical wave. A sinusoidal wave

representing this solution in physical reality can be extracted from Equation (1.13) using *Euler's formula*, yielding

$$\psi(\mathbf{r}, t) = \operatorname{Re} [\hat{\Psi}_0 \exp [i(\hat{\mathbf{k}} \cdot \mathbf{r} - \omega t + \delta)]] = \operatorname{Re} [\hat{\psi}(\mathbf{r}, t)]. \quad (1.14)$$

Remark 1.2.2. Clearly, if Equation (1.14) satisfies equations (1.11) and Maxwell's equations, the same holds true for Equation (1.13), as the imaginary part differs from the real part only by the replacement of sine with cosine.

Equation (1.13) serves as an established elementary solution to the general wave equation and hence also to equations (1.11). Substituting this solution into equations (1.10), it becomes evident that these "lossy wave equations" also admit plane-wave solutions. Furthermore, this substitution allows for deriving a general formula for the complex *wavenumber* of a plane wave:

$$\hat{k}^2 = \hat{\mathbf{k}} \cdot \hat{\mathbf{k}} = \mu\epsilon\omega^2 + i\mu\sigma\omega. \quad (1.15)$$

In the context of Equation (1.13), it is evident that the real part of the complex wavenumber \hat{k} is the *actual* wavenumber as it determines the change of phase with spatial propagation. For this reason, the real part is simply denoted k and is called the *phase constant*. In contrast, the imaginary part of \hat{k} is responsible for the exponential damping, or attenuation, in conductive media and hence is called the *attenuation constant*.

Waves described by Equation (1.13) are called *monochromatic*, or *time-harmonic*, *plane* waves. Monochromaticity refers to the wave oscillating at a single frequency ω through time, while planarity indicates that the fields are uniform over every plane perpendicular to the direction of propagation. Although less common, plane waves could alternatively be called *space-harmonic*,³ as both terms signify a sinusoidal dependence on a given variable. In the case of monochromaticity, the variable is time, oscillating with an angular frequency ω . Similarly, planarity reflects the waveform repetition in the spatial coordinates, projected into the propagation direction, with a well-defined spatial frequency k .

The significance of this particular solution stems from the fact that, in practice, any wave relevant to engineering purposes can be expressed as a linear combination of these monochromatic plane waves, i.e.,

$$\hat{\psi}(\mathbf{r}, t) = \int_{\mathbb{R}^3} \hat{\Psi}_0(\mathbf{k}) \exp [i(\hat{\mathbf{k}} \cdot \mathbf{r} - \omega t)] d\mathbf{k}. \quad (1.16)$$

This superposition principle mathematically reflects the Fourier transform over every plane wave corresponding to a given frequency ω . With this formally sound mathematical description, the existence of a unique linear combination for "any wave relevant to engineering purposes", as vaguely stated above, can be rigorously established.

Indeed, since any physically realizable signal is square-integrable and has compact support,⁴ the existence of its Fourier transform is guaranteed. This implication is granted by recalling that the combination of square integrability and compact support implies absolute integrability by the Cauchy-Schwarz inequality, which forms a sufficient condition for the existence of the Fourier transform. Therefore, any such physical signal

³Therefore, monochromatic plane waves are something one could call *spacetime-harmonic* or simply *harmonic*.

⁴In the field of signal processing, these signal properties are often described as having *finite energy* and *duration*, respectively.

can be confidently decomposed into a superposition of monochromatic plane waves, as expressed in Equation (1.16). This decomposition into a unique linear combination of plane waves of different frequencies underpins much of the mathematical theory concerning Fourier analysis. For a deeper dive into the mathematical foundations of Fourier integrals, [8] can be consulted. Furthermore, a formulation of Dirichlet conditions, which are more relevant to signal processing applications, can be found in [9].

Because the focus of this text is confined to physically realizable signals, i.e., signals possessing these crucial properties, a restriction of our attention to monochromatic plane waves is justified. Therefore, fields taking on the form of

$$\hat{\mathbf{E}}(\mathbf{r}, t) = \hat{\mathbf{E}}_0 \exp \left[i \left(\hat{\mathbf{k}} \cdot \mathbf{r} - \omega t \right) \right], \quad (1.17a)$$

$$\hat{\mathbf{B}}(\mathbf{r}, t) = \hat{\mathbf{B}}_0 \exp \left[i \left(\hat{\mathbf{k}} \cdot \mathbf{r} - \omega t \right) \right] \quad (1.17b)$$

are considered, where $\hat{\mathbf{E}}_0$ and $\hat{\mathbf{B}}_0$ are complex amplitudes.

As discussed in Remark 1.2.1, satisfying the wave equations does not guarantee solutions to Maxwell's equations. Substituting the solutions of the wave equations into Maxwell's equations is necessary, as it might refine the solutions or yield more information. For example, consider plane waves in a vacuum.

Example 1.2.3 [Monochromatic plane waves in free space]. Substituting Equations (1.17a) and (1.17b) for the electric and magnetic field in the free-space version of Equations (1.9a) and (1.9c) read

$$\mathbf{k} \cdot \hat{\mathbf{E}}_0 = \mathbf{k} \cdot \hat{\mathbf{B}}_0 = 0, \quad (1.18)$$

i.e., the electromagnetic fields are *transverse*. Furthermore, either of Equations (1.9b) and (1.9d) yields

$$\hat{\mathbf{B}}_0 = \frac{1}{\omega} (\mathbf{k} \times \hat{\mathbf{E}}_0) = \frac{1}{c} (\mathbf{e}_k \times \hat{\mathbf{E}}_0). \quad (1.19)$$

Clearly, in free space, \mathbf{E} and \mathbf{B} are *mutually perpendicular* and *in phase*, meaning their oscillations reach their peaks and troughs simultaneously.

A *polarization vector* is introduced to further characterize the plane wave. This unit vector points in the direction of electric field oscillations, i.e.,

$$\mathbf{e}_n \cdot \mathbf{E} = \mathbf{E} \quad \|\mathbf{e}_n\| = 1. \quad (1.20)$$

With this definition, the complete solution to Maxwell's equations for a plane wave in free space takes the form of

$$\mathbf{E}(\mathbf{r}, t) = E_0 \cos(\mathbf{k} \cdot \mathbf{r} - \omega t + \delta) \mathbf{e}_n, \quad (1.21)$$

$$\mathbf{B}(\mathbf{r}, t) = \frac{1}{c} E_0 \cos(\mathbf{k} \cdot \mathbf{r} - \omega t + \delta) (\mathbf{k} \times \mathbf{e}_n). \quad (1.22)$$

It's important to note that this transversality of the electromagnetic fields is a specific property of plane waves in free space or lossless media. When waves are confined in waveguides or propagate through lossy media, the fields generally have longitudinal components as well. This distinction arises because the boundary conditions imposed by the waveguide or the interactions with the medium can alter the field structure.

1.2.3 Polarization

A brief examination of the general polarization properties of monochromatic plane waves is now undertaken. For the sake of simplicity, consideration is restricted to propagation within a vacuum. Consequently, the Cartesian coordinate system is aligned such that the unit vector e_z coincides with the unit vector e_k , which defines the direction of propagation. The remaining real unit vectors, e_x and e_y , are then defined such that (e_x, e_y, e_z) constitutes a right-handed orthogonal triad of unit vectors. Thus, the ordered set of vectors (e_x, e_y) forms a basis for the complex amplitude of the electric field \mathbf{E} , and the electric field can thereby be expressed as

$$\hat{\mathbf{E}}(\mathbf{r}, t) = [\hat{E}_x \mathbf{e}_x + \hat{E}_y \mathbf{e}_y] \exp [i\phi(\mathbf{r}, t)], \quad (1.23)$$

where

$$\hat{E}_x = E_x \exp(i\delta_x), \quad \hat{E}_y = E_y \exp(i\delta_y), \quad (1.24)$$

for some real numbers E_x , E_y , δ_x , and δ_y , and

$$\phi(\mathbf{r}, t) = \hat{\mathbf{k}} \cdot \mathbf{r} - \omega t. \quad (1.25)$$

Expressing the real part of Equation (1.23) yields

$$\text{Re} [\hat{\mathbf{E}}] = E_x \cos(\phi + \delta_x) \mathbf{e}_x + E_y \cos(\phi + \delta_y) \mathbf{e}_y = A_x \mathbf{e}_x + A_y \mathbf{e}_y. \quad (1.26)$$

Equating the components from the second relation in Equation (1.26) and applying goniometric identities, the following relationships are obtained:

$$\frac{A_x}{E_x} \sin(\delta_y) - \frac{A_y}{E_y} \sin(\delta_x) = \sin(\delta_y - \delta_x) \cos(\phi), \quad (1.27a)$$

$$\frac{A_x}{E_x} \sin(\delta_y) - \frac{A_y}{E_y} \sin(\delta_x) = \sin(\delta_y - \delta_x) \cos(\phi). \quad (1.27b)$$

Subsequent squaring and addition of Equations (1.27a) and (1.27b) yields

$$\left(\frac{A_x}{E_x} \right)^2 + \left(\frac{A_y}{E_y} \right)^2 - 2 \frac{A_x}{E_x} \frac{A_y}{E_y} \cos(\delta) = \sin^2(\delta), \quad (1.28)$$

where $\delta \equiv \delta_y - \delta_x$. Clearly, Equation (1.28) defines an ellipse in the plane transverse to the propagation direction. Accordingly, the general monochromatic plane wave described in Equation (1.13) exhibits *elliptical polarization*. The eccentricity and orientation of the ellipse are related to the phase difference δ and the amplitude ratio E_y/E_x . Upon inspecting Equation (1.28), two special types of polarization can be identified for specific parameter values.

Linear polarization. The first situation arises when the polarization ellipse degenerates into a straight line. This condition occurs when the electric field components are either in-phase or out-of-phase by half-wavelength, i.e.,

$$\delta = \delta_y - \delta_x = m\pi, \quad m \in \mathbb{N}_0. \quad (1.29)$$

This situation corresponds to *linear polarization* and Equation (1.26) is rendered as

$$\text{Re} [\hat{\mathbf{E}}(\mathbf{r}, t)] = [E_x \mathbf{e}_x \pm E_y \mathbf{e}_y] \cos(\phi + \delta_x). \quad (1.30)$$

Circular polarization. The alternative scenario arises when the polarization ellipse simplifies into a circle. This simplification occurs exclusively when the orthogonal electric field components possess equal amplitude and are out-of-phase by one-quarter wavelength, i.e.,

$$E_x = E_y = \frac{E}{\sqrt{2}}, \quad \delta = \delta_y - \delta_x = (2m + 1)\frac{\pi}{2}, \quad m \in \mathbb{Z}. \quad (1.31)$$

This condition corresponds to *circular polarization*, as the tip of the polarization vector traces a circle within every fixed transverse plane. The plane $z = 0$ is considered to ascertain the direction of circular movement. By setting $\delta_x = 0$,⁵ Equation (1.26) is expressed as

$$\text{Re} \left[\hat{\mathbf{E}}_{\pm}(\mathbf{0}, t) \right] = \frac{E}{\sqrt{2}} [\cos(\omega t) \mathbf{e}_x \pm \sin(\omega t) \mathbf{e}_y]. \quad (1.32)$$

This expression demonstrates that when viewed from the direction defined by $\hat{\mathbf{k}}$, the electric field $\hat{\mathbf{E}}^+$ represents a circularly polarized wave with the polarization vector rotating anticlockwise, thus defining *left-hand circular polarization* (LHCP). Conversely, the case of $\hat{\mathbf{E}}^-$ represents a circularly polarized wave with the polarization vector rotating clockwise, defining *right-hand circular polarization* (RHCP).

The exposition given so far is aligned with Augustin-Jean Fresnel's general definition of elliptical polarization, as presented in his memoir to the French Academy of Sciences on 9 December 1822, wherein the concepts of the three types of polarization—general elliptical polarization, and its specific forms, linear and circular polarization—were coined. The following remark, however, provides an alternative and often advantageous approach.

Remark 1.2.4 [Complex basis for circular polarization]. For the electric field decomposition basis in Equation (1.23), the following complex conjugate vectors, rather than the Cartesian vectors \mathbf{e}_x and \mathbf{e}_y , are now considered:

$$\mathbf{e}_+ = \frac{1}{\sqrt{2}} (\mathbf{e}_x + i\mathbf{e}_y), \quad \mathbf{e}_- = \frac{1}{\sqrt{2}} (\mathbf{e}_x - i\mathbf{e}_y). \quad (1.33)$$

These vectors maintain orthonormality. Using this basis, it is evident that the real part of the thus-formed complex electric field

$$\hat{\mathbf{E}}_{\pm}(\mathbf{r}, t) = E \mathbf{e}_{\pm} \exp \left[i \left(\hat{\mathbf{k}} \cdot \mathbf{r} - \omega t \right) \right] = \frac{E}{\sqrt{2}} [\mathbf{e}_x \pm i\mathbf{e}_y] \exp \left[i \left(\hat{\mathbf{k}} \cdot \mathbf{r} - \omega t \right) \right], \quad (1.34)$$

evaluated at $\mathbf{r} = 0$, is equivalent to Equation (1.32). Because the ordered set of vectors defined by Equation (1.33) constitutes a valid basis for the transverse plane, analogous to the $(\mathbf{e}_x, \mathbf{e}_y)$ basis, the expression

$$\hat{\mathbf{E}} = [E_+ \mathbf{e}_+ + E_- \mathbf{e}_-] \exp [i\phi] \quad (1.35)$$

is an equivalent representation to Equation (1.23). Consequently, any monochromatic plane wave can be decomposed into RHCP and LHCP components analogous to its decomposition into orthogonal linearly polarized components.

⁵The choice $\delta_x = 0$ is inconsequential to the resulting polarization as it depends only on the phase difference δ .

1.2.4 Guided waves

The behaviour of electromagnetic waves within a waveguide is now explored. An assumption is made to provide a clear framework for analysis that the waveguide walls are perfect electric conductors (PEC), implying the absence of surface sources. This idealization leads to specific boundary conditions

$$\mathbf{e}_n \times \mathbf{E} = 0, \quad (1.36a)$$

$$\mathbf{e}_n \cdot \mathbf{B} = 0. \quad (1.36b)$$

It is essential to recognize that free charges and currents will be induced on the surface precisely to enforce these constraints.

Furthermore, the focus is on monochromatic plane waves propagating along the waveguide. This implies that the electric and magnetic fields have a harmonic time dependence with a single angular frequency ω . The \hat{k} notation is dispensed with as \hat{k} is real for the cases of interest. The general form of the fields is then given by equations (1.17), where the z -axis is aligned with the waveguide's longitudinal direction. The complex amplitudes of the fields,

$$\hat{\mathbf{E}}_0 = E_x \mathbf{e}_x + E_y \mathbf{e}_y + E_z \mathbf{e}_z, \quad (1.37a)$$

$$\hat{\mathbf{B}}_0 = B_x \mathbf{e}_x + B_y \mathbf{e}_y + B_z \mathbf{e}_z, \quad (1.37b)$$

are functions of the transverse coordinates, x and y , reflecting the spatial variations of the fields within the waveguide cross-section.

To further simplify the analysis, the waveguide is considered source-free, meaning that no free charges or currents are *impressed* within the waveguide. This allows the utilization of the simplified form of Maxwell's equations (1.9). Due to the assumed linearity of the medium within the waveguide, these equations are expressed in terms of \mathbf{E} and \mathbf{B} .

With these assumptions in place, the behaviour of guided waves can be analysed. From Equations (1.9b) and (1.9d), adapted for a linear medium, a set of coupled differential equations relating the transverse components of the electric and magnetic fields is obtained. These equations can be solved to express the transverse field components in terms of the longitudinal components, taking the form of

$$E_x = \zeta (k \partial_x E_z + \omega \partial_y B_z), \quad (1.38a)$$

$$B_x = \zeta \left(k \partial_x B_z - \frac{\omega}{c^2} \partial_y E_z \right), \quad (1.38c)$$

$$E_y = \zeta (k \partial_y E_z - \omega \partial_x B_z), \quad (1.38b)$$

$$B_y = \zeta \left(k \partial_y B_z + \frac{\omega}{c^2} \partial_x E_z \right), \quad (1.38d)$$

where $\zeta = i/((\omega/c)^2 - k^2)$. Finally, substituting equations (1.38) into Equations (1.9a) and (1.9c) yields the uncoupled equations

$$\left[\partial_x^2 + \partial_y^2 + \left(\frac{\omega}{c} \right)^2 - k^2 \right] E_z = 0, \quad (1.39a)$$

$$\left[\partial_x^2 + \partial_y^2 + \left(\frac{\omega}{c} \right)^2 - k^2 \right] B_z = 0. \quad (1.39b)$$

These equations, often referred to as the *Helmholtz equations*, govern the longitudinal field components and play a crucial role in determining the allowed modes of propagation within the waveguide. These modes are categorized based on the presence or absence of longitudinal components in the electric and magnetic fields. *Transverse electric* (TE) waves have $E_z = 0$, while *transverse magnetic* (TM) waves have $B_z = 0$. The simplest waves, for which both $E_z = B_z = 0$, are called *transverse electromagnetic* (TEM) waves, but these cannot exist within a hollow waveguide due to boundary conditions.

Remark 1.2.5 [Non-existence of TEM waves in hollow waveguides]. To further illustrate this point, consider the case of a waveguide with perfectly conducting walls.

Beginning with the scenario where the longitudinal component of the electric field, E_z , is zero, it follows from Equation (1.9a) that the divergence of the electric field in the transverse plane must also be zero. Similarly, when the longitudinal component of the magnetic field, B_z , is zero, Equation (1.9b) dictates that the curl of the electric field in the transverse plane must vanish.

Combining these results, the complex amplitude of the electric field, $\hat{\mathbf{E}}_0$, can be expressed as the gradient of a scalar potential φ that satisfies Laplace's equation $\Delta\varphi = 0$. However, the boundary condition on the electric field, as expressed in Equation (1.36a), enforces an equipotential at the conductor surface. Since the solution to Laplace's equation is unique given the boundary conditions, and the boundary condition enforces an equipotential, the potential must be constant throughout the waveguide. Thus, the electric field must be zero.

Remark 1.2.6 [Modal decomposition of guided waves]. The equations (1.39) for E_z and B_z are instances of the *Helmholtz equation* with Dirichlet and Neumann boundary conditions, respectively. This mathematical structure is the eigenvalue problem for the Laplace operator arising in various physical contexts.

For instance, the same equation and boundary conditions govern the vertical displacements of a vibrating drumhead. In this analogy, TM modes correspond to a drumhead with fixed boundaries, while TE modes correspond to a drumhead with free boundaries. The TM case is also isomorphic to the Schrödinger problem for a free particle's wave functions and energy eigenvalues in a two-dimensional box with rigid walls. Seeking inspiration in these analogous problems provides valuable intuition when thinking about a waveguide's modal eigenfunctions and eigenvalues. Some key mathematical results stemming from these analogies include:

- (a) There are infinite TE- and TM-mode eigenfunctions.
- (b) The eigenvalues are all real and positive.
- (c) The eigenfunctions can always be chosen real.
- (d) The eigenfunctions form a complete set of functions.
- (e) Eigenfunctions belonging to different eigenvalues are orthogonal, i.e.,

$$\int_S \left[\hat{\mathbf{E}}_{0,\alpha} \times \hat{\mathbf{B}}_{0,\beta}^* \right] dS = C\delta_{\alpha\beta}, \quad (1.40)$$

where S is an arbitrary waveguide cross-section and $\delta_{\alpha\beta}$ is the Kronecker's delta distribution.

The most significant result in terms of applied electrodynamics is the completeness of the eigenfunctions, which implies that any field within a waveguide can be composed of its modes. Specifically, if α denotes a distinct mode,⁶ then any wave travelling in the positive direction (denoted by the + superscript) can be decomposed as

$$\hat{\mathbf{E}}^+ = \sum_{\alpha} C_{\alpha}^+ \left[\hat{\mathbf{E}}_{0,\alpha} + \mathbf{e}_z E_{z,\alpha} \right] \exp(-ik_{\alpha} z), \quad (1.41)$$

$$\hat{\mathbf{B}}^+ = \sum_{\alpha} C_{\alpha}^+ \left[\hat{\mathbf{B}}_{0,\alpha} + \mathbf{e}_z B_{z,\alpha} \right] \exp(-ik_{\alpha} z). \quad (1.42)$$

⁶For example, in the case of a rectangular waveguide, a mode is given by the combination of two integers, m and n .

Similarly, for the negative direction (denoted by the $-$ superscript), the decomposition is given by

$$\hat{\mathbf{E}}^- = \sum_{\alpha} C_{\alpha}^- \left[\hat{\mathbf{E}}_{0,\alpha} - \mathbf{e}_z E_{z,\alpha} \right] \exp(i k_{\alpha} z), \quad (1.43)$$

$$\hat{\mathbf{B}}^- = \sum_{\alpha} C_{\alpha}^- \left[-\hat{\mathbf{B}}_{0,\alpha} + \mathbf{e}_z B_{z,\alpha} \right] \exp(i k_{\alpha} z). \quad (1.44)$$

Furthermore, thanks to the mutual orthogonality of modes, the modal decomposition is uniquely given by the orthogonal projection

$$C_{\alpha}^{\pm} = \frac{1}{2} \frac{\int_S \left[\hat{\mathbf{E}}_{0,\alpha}^* \cdot \hat{\mathbf{E}} \pm \left(\frac{\omega}{k_{\alpha}} \right)^2 \hat{\mathbf{B}}_{0,\alpha}^* \cdot \hat{\mathbf{B}} \right] dS}{\int_S \hat{\mathbf{E}}_{0,\alpha}^* \cdot \hat{\mathbf{E}}_{0,\alpha} dS} \exp(\pm i k_{\alpha} z), \quad (1.45)$$

where S is an arbitrary cross-section of the waveguide.

These two results combined lead to a powerful conclusion: the tangential fields within an arbitrary cross-section of the waveguide fully determine the field everywhere within the waveguide. This means that if the tangential components of the electric and magnetic fields are known on a single transverse plane, the entire field distribution within the waveguide can be uniquely determined, both in the transverse plane and along the direction of propagation.

Example 1.2.7 [TE waves in a rectangular waveguide]. This example explores the specific case of TE waves within a rectangular waveguide. A waveguide with height a in the x -direction and width b in the y -direction is considered, the z -axis again being aligned with the waveguide's longitudinal direction. The objective is to derive an expression for the longitudinal component of the magnetic field, B_z , using the method of separation of variables. This method involves assuming that, for every x and y , $B_z(x, y)$ can be expressed as the product of two independent functions, $X(x)$ and $Y(y)$.

Substituting this product into Equation (1.39b) yields a differential equation that can be rearranged by dividing through by B_z . This rearranged equation reveals that the x -dependent and y -dependent terms must be constant, leading to two ordinary differential equations,

$$\frac{1}{X} X'' = -k_x^2, \quad (1.46a)$$

$$\frac{1}{Y} Y'' = -k_y^2. \quad (1.46b)$$

Additionally, a relationship between the separation constants, k_x and k_y , and the wave number, k , is established:

$$-k_x^2 - k_y^2 + \left(\frac{\omega}{c} \right)^2 - k^2 = 0. \quad (1.47)$$

Equation (1.46a) is a simple second-order ordinary differential equation with a general solution

$$X(x) = A \sin(k_x x) + B \cos(k_x x). \quad (1.48)$$

Furthermore, boundary conditions must be applied to determine the particular solution. The boundary condition (1.36b) enforces the vanishing of B_x at $x = 0$ and $x = a$. According to Equation (1.38c), this translates to enforcing the vanishing of $\partial_x B_z = X'$

at those points. This implies $A = 0$ and the separation constant k_x must satisfy the condition

$$k_x = \frac{m\pi}{a}, \quad m \in \mathbb{N}_0. \quad (1.49)$$

Similarly, for the function $Y(y)$, the boundary condition leads to the condition

$$k_y = \frac{n\pi}{b}, \quad n \in \mathbb{N}_0. \quad (1.50)$$

Combining these results, the particular solution for B_z takes the form of

$$B_z(x, y) = B_0 \cos\left(\frac{m\pi}{a}x\right) \cos\left(\frac{n\pi}{b}y\right), \quad (1.51)$$

representing the TE_{mn} wave with the corresponding wavenumber given by Equation (1.47). This information is a complete solution to the wave propagation since the remaining field components are provided by equations (1.38).

Examining Equation (1.47), it becomes evident that if the frequency falls below a specific *cutoff frequency*,

$$f_{mn} \equiv \frac{c}{2} \sqrt{\left(\frac{m}{a}\right)^2 + \left(\frac{n}{b}\right)^2}, \quad (1.52)$$

the wavenumber becomes imaginary. This signifies that the wave cannot propagate and instead decays exponentially within the waveguide. Such solutions are referred to as *evanescent waves*. This cutoff frequency depends on the mode numbers (m, n) and the waveguide dimensions (a, b) . Modes having the same cutoff frequency are called *degenerate*.

The wavelength corresponding to wavenumber k in the direction of guided wave propagation is called the *guide wavelength* and is given by

$$\lambda_g \equiv \frac{2\pi}{k} = \frac{\lambda}{\sqrt{1 - \left(\frac{f_{mn}}{f}\right)^2}} = \frac{\lambda}{\sqrt{1 - \left(\frac{\lambda}{\lambda_{mn}}\right)^2}}. \quad (1.53)$$

This guide wavelength is related to the free-space wavelength, λ , and the cutoff wavelength, λ_{mn} , for the TE_{mn} mode.

The analysis presented in this chapter establishes the fundamental principles governing electromagnetic wave propagation in waveguides, with a particular focus on rectangular geometries. The concept of cutoff frequency, below which waves become evanescent, has been introduced, and its dependence on waveguide dimensions and mode numbers has been highlighted. This understanding is crucial for the design of waveguide-based components, as it dictates the operational frequency range and the selection of appropriate waveguide dimensions to support the desired modes. Furthermore, the distinction between propagating and evanescent modes is essential for optimizing the performance of the polarizer and the feeding structure, which will be discussed in subsequent chapters. By carefully considering the cutoff frequencies of different modes, the design can be tailored to ensure that only the desired modes propagate efficiently while undesired modes are effectively suppressed. This modal selectivity is key in achieving high polarization purity and minimizing signal loss in the overall antenna system.

Chapter 2

Polarizer

The design process of a waveguide polarizer is detailed in this chapter. An initial survey of existing literature, including relevant conference papers and research articles, is undertaken. Based on this survey, the performance characteristics of various design concepts are compared and contrasted. A solution to the design problem is proposed, with a rationale for the selected approach. Following this selection, an in-depth eigen-mode analysis of the chosen structure is performed. As demonstrated in this chapter, this analysis yields crucial insights into the operational principles, allows for the recognition of key performance parameters, and provides the foundation for defining the optimization problem. The chosen structure is subsequently implemented and optimized within CST Studio Suite for a specified target frequency band. The inherent trade-offs between key performance parameters are then discussed with reference to established principles of guided wave propagation in rectangular waveguides. Finally, the simulated performance of the designed component is presented graphically, derived from full-wave simulations.

2.1 Principle of operation

Typically, the inherent characteristics of symmetric waveguides are leveraged to achieve dual polarization. This choice stems from their unique ability to enable independent control over two orthogonal polarization states possessing identical propagation characteristics. Such independent control is essential for polarization manipulation, facilitating the adjustment of these orthogonal modes' relative phase and amplitude to achieve the desired polarization states. This capability is applied directly in the design of the dual linear-to-circular polarizer detailed herein. The desired polarization states of RHCP and LHCP were elaborated on mathematically in Section 1.2.1.

This crucial characteristic arises from two fundamental properties rooted in the electrodynamics of symmetric waveguides. Firstly, their geometric symmetry, manifesting as mirror or rotational symmetry, permits the existence of two fundamental degenerate modes. As illustrated in Example 1.2.7, a square waveguide exhibits this characteristic with its TE_{10} and TE_{01} modes. Secondly, as detailed in Remark 1.2.6, a fundamental principle derived from Maxwell's equations dictates that any two distinct modes within a waveguide are mutually orthogonal. This orthogonality expressed mathematically in Equation (1.40), ensures that the power flow associated with the interaction of any two distinct modes is zero. In essence, transverse symmetry enables the existence of orthogonally polarized modes, while their inherent orthogonality ensures their independent propagation without coupling or interference.

The description of circular polarization expressed compactly in Equation (1.31) establishes a clear objective for the design of a waveguide polarizer: the creation of a segment, based on a symmetrical waveguide, that introduces a one-quarter wavelength phase difference between the two orthogonal modes along its length while maintaining equal magnitudes. In subsequent design stages, this latter criterion is quantified by a singular metric known as the *axial ratio* of the emitted wave, characterizing the polarization purity based on its far-field properties. Several widely adopted approaches exist for achieving these objectives; these may be referred to as standard methods. Notable examples include the following:

- *Dielectric vane polarizers* utilize a dielectric element (a so-called quarter-wave plate) inserted into a segment of a symmetrical waveguide at an angle of $\pm 45^\circ$ relative to the incident electric field. The inserted dielectric introduces a difference in the propagation velocities of the two orthogonal modes along this segment. This differential propagation velocity arises from the interaction of one mode with the vane, which reduces its propagation velocity due to its parallel orientation relative to the vane. In contrast, the orthogonal mode remains unaffected due to its perpendicular orientation.
- *Septum polarizers* comprise two rectangular ports converging at a stepped septum and extending into a symmetrical waveguide. When the structure is excited through one of these ports, the septum polarizer converts approximately half of the incident energy to the orthogonal polarization, achieving circular polarization by introducing a one-quarter wavelength phase shift at the output port. Excitation of the structure through the alternate port results in circular polarization of the opposite handedness.
- *Iris polarizers* utilize symmetrical waveguides with non-trivial cross-sections, incorporating ridges, also called corrugations or irises, typically positioned symmetrically on two opposing sides. These polarizers operate on a linearly polarized wave incident diagonally into the waveguide. In this configuration, the ridges present inductive characteristics to one of the waveguide modes and capacitive characteristics to the orthogonal mode. This differential interaction results in a one-quarter wavelength phase delay at the output port.

2.2 Literature survey

While the methods established above can be refined and adjusted to achieve favourable results in typical metrics for linear-to-circular polarizers, each also exhibits inherent limitations. While simple to implement, dielectric vane polarizers encounter narrow bandwidth issues and suffer from significant power limitations due to inherent dielectric losses. The dielectric losses are encompassed in Equation (1.15) as any real dielectric exhibits a small but non-zero conductivity $\sigma > 0$. These losses become particularly pronounced at higher frequencies and power levels, restricting their applicability in certain scenarios. In contrast, septum polarizers offer promising capabilities for a wide range of applications, particularly in power handling and the efficient generation of both right-hand and left-hand circular polarization. As noted by [10], modifications to septum designs, such as integrating RF MEMS switches, can effectively achieve reconfigurability and control over the handedness of the produced circular polarization. However, the size and weight of septum structures can pose significant constraints, especially in compact or weight-sensitive applications. Furthermore, as highlighted

by [11], alternative septum geometries, such as tapered slots, while offering potential design variations, do not necessarily demonstrate substantial performance improvements over conventional stepped septum designs. While capable of converting linearly polarized input into circular polarizations and operating at higher power levels, iris polarizers often exhibit challenges related to “overmoding” within their structures, necessitating precise mode-matching to maintain a satisfactory axial ratio across a broad frequency band. As observed by [12], variations in iris design, such as incorporating ridges on four sides instead of two, can be explored. Moreover, as emphasized by [13], the design of iris arrays requires extensive analysis of the optimal geometry, often involving complex mathematical techniques, to achieve desired performance characteristics. This complexity is further compounded when considering wider bandwidth operation, as noted by [14], which may necessitate cascading individual sections and careful consideration of different ridge types and transmission matrix approaches. Finally, as demonstrated by [15], innovative manufacturing techniques, such as additive manufacturing, combined with alternative waveguide geometries like triangular waveguides, offer potential avenues for further advancement in polarizer design, encompassing design, manufacturing, and measurement aspects.

An approach diverging from these standard methods is designing waveguide geometries utilizing mode dispersion to manipulate electromagnetic waves. Two prominent examples of modified waveguides include elliptical and waveguides with shaped metallic inserts. As demonstrated in [16], in the context of a wideband circularly polarized horn antenna, elliptical waveguides leverage their inherent anisotropy to induce the required phase shift. The use of tapered elliptical waveguides, as also explored in [16], facilitates wideband operation. On the other hand, waveguides with shaped metallic inserts introduce field perturbations to achieve the desired polarization transformation. As shown in [17]–[20], these inserts can take various forms, including square or triangular blocks inserted into diagonally opposite corners of a square waveguide. Due to the modified geometry and resulting boundary conditions of such waveguides, their modes experience variations in their transverse field distributions and, consequently, their effective transverse wavenumbers. This difference in transverse wavenumbers necessitates a corresponding difference in their longitudinal wavenumbers, or phase constants, to satisfy the waveguide’s dispersion relation, which links the transverse and longitudinal wavenumbers. Consequently, an accumulative phase difference develops between the modes as they propagate along the length of the polarizer. Furthermore, as explored in [21], more optimal cross-sectional shapes, such as a bow-tie configuration, can enhance performance, although often at the expense of increased manufacturing complexity. While the higher frequency regions targeted in most of the explored articles are not the primary focus of this work, the underlying principles of achieving polarization control through modified waveguide cross-sections provide valuable insights and inspiration for the design of the polarizer presented herein.

Selected approach. This thesis introduces a novel approach to achieving enhanced polarization purity using a straightforward and robust cross-sectional geometry. This geometry is realized by inserting simple shapes into two opposing sides of a waveguide’s cross-section. Initially, both square and circular waveguides, each suitable for dual linear-to-circular polarization conversion, are examined and compared to determine the more advantageous geometry. For the square waveguide illustrated in Figure 2.1a, triangular prisms are inserted into two opposing corners, forming a hexagonal waveguide studied in [18]. At the same time, cylindrical segments are used for the circular waveguide in Figure 2.1b. This concept is inspired by the established technique of achieving circular polarization with a square patch antenna by chamfering its opposing corners. The

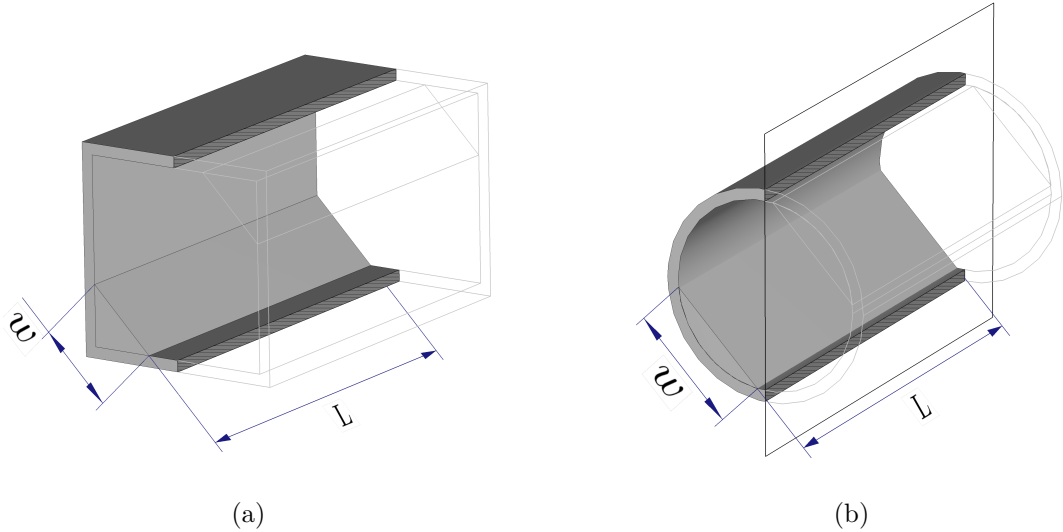


Figure 2.1: Symmetric polarizers: models

resulting cross-sections can be considered Babinet-complementary¹ to this antenna configuration.

This approach was selected primarily for its relative ease of fabrication, particularly at higher frequencies, and its potential for adaptation to various frequency bands. However, due to the resonant, and hence geometry-dependent, nature of the mode dispersion introduced by the metallic inserts, optimal performance is anticipated over a moderately wide bandwidth rather than an ultrawide one. This bandwidth limitation represents a trade-off for the design's simplicity, robustness, and manufacturability. Triangular prisms, in particular, simplify fabrication compared to more complex curved geometries while providing effective field manipulation for polarization control.

2.3 Eigenmode analysis

The focus now shifts to the *eigenmode analysis* of the two waveguides illustrated in Figure 2.1. This powerful technique, based on the theory outlined in Remark 1.2.6, facilitates the establishment of figures of merit intrinsic to polarizing structures, enabling performance tracking and aiding in the determination of the more advantageous geometry.

Initially, the fundamental propagation modes in the symmetric waveguides are considered *without* the inserted shapes. In the case of the square waveguide, it is the TE₁₀ and TE₀₁ modes illustrated in Figures 2.2a and 2.2b, whereas the two degenerate TE₁₁ modes² of the circular waveguide are presented in Figures 2.2c and 2.2d. For both waveguides individually, these two degenerate modes represent the waves launched into the polarizer via a standard waveguide section. Upon encountering the metallic inserts, incident waves can no longer be represented by the eigenmodes of the simple waveguide structure; their energy is coupled into a linear combination of the fundamental eigenmodes of the respective polarizer.

¹This name refers to the notion of complementary structures according to *Babinet's principle*, derivation of which is out of scope for this text. More details can be found, e.g., in [22].

²Note that circular waveguides possess an infinite number of degenerate TE₁₁ modes due to their rotational symmetry. Here, two are chosen for their perpendicular oscillations which aligns well with the definition of circular polarization in Section 1.2.3.

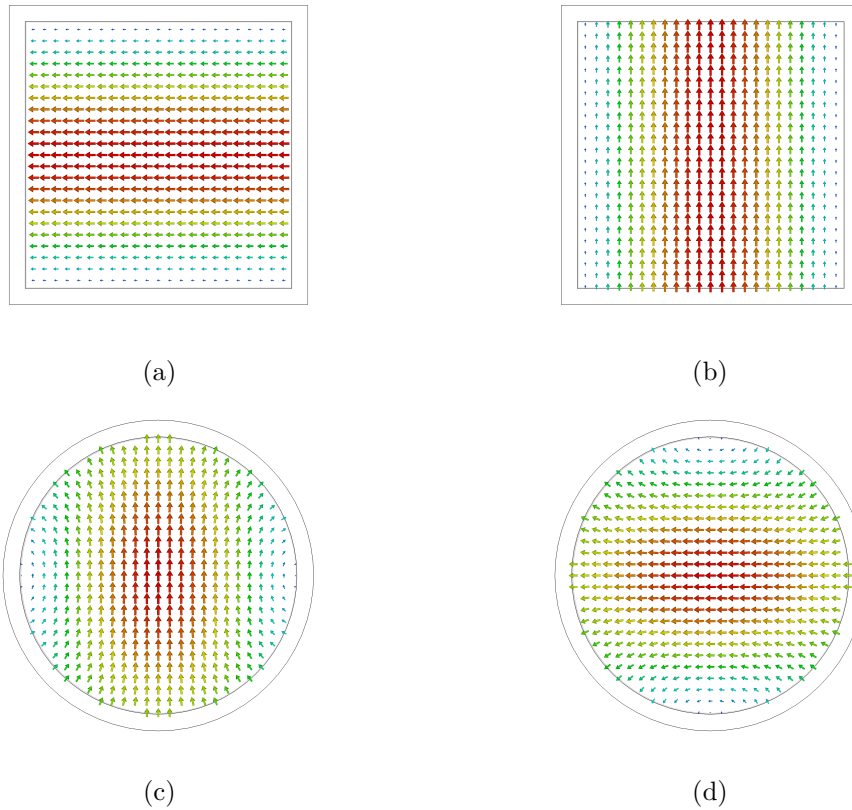


Figure 2.2: Symmetric waveguides: fundamental modes

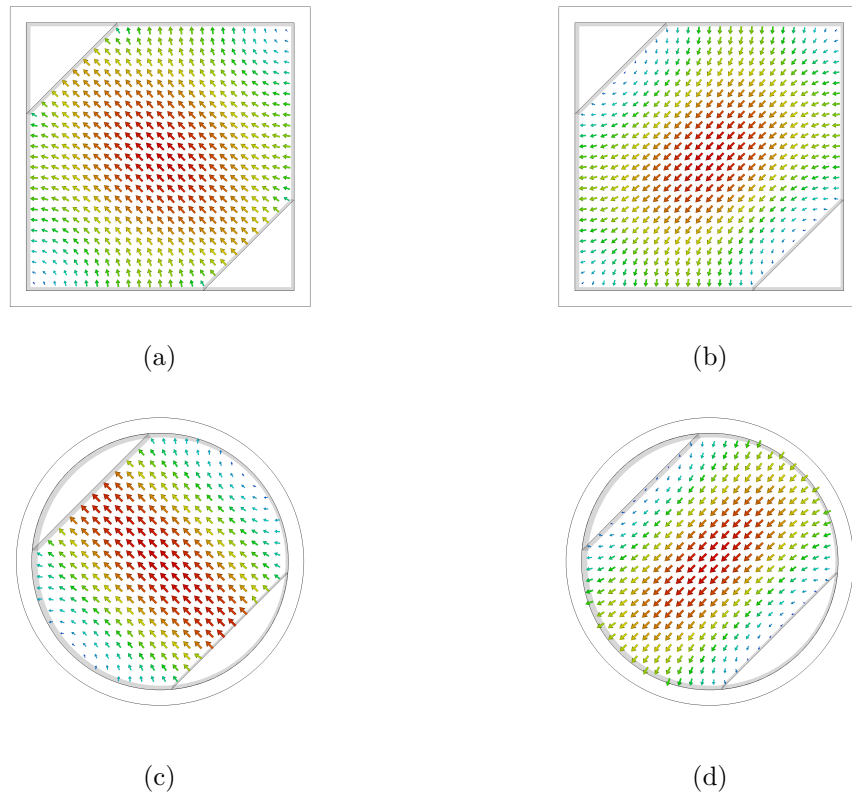


Figure 2.3: Symmetric polarizers: fundamental modes

With the incident modes established, the eigenmodes of the polarizers, which are the identical waveguides but now *with* the shapes inserted, are analysed. The eigenmodes take the form presented in Figures 2.3a and 2.3b for the square geometry, whereas the circular waveguide with inserts supports two fundamental modes depicted in Figures 2.3c and 2.3d. As expected, the transverse field exhibits a standing wave behaviour in both cases as dictated by the boundary conditions on a conductive surface. More importantly, for the polarization transformation, the metallic shapes perturb the electromagnetic fields, changing the propagation constants of the existing modes. Crucially, the presence of these inserts breaks the original symmetry of the waveguide, causing a dispersion, or difference in phase velocity, between the two fundamental modes of propagation. This fact is illustrated in Figure 2.3, wherein in both geometries, one of the modes perceives a different electric path than the other. This dispersion is the key mechanism for achieving circular polarization. The phase difference between the two fundamental modes accumulates as the electromagnetic wave propagates along the waveguide. This cumulative phase lag can be precisely controlled by carefully selecting the geometry and placement of the inserts and the length of the waveguide. In the context of a polarizer designed to generate circular polarization, the goal is to achieve precisely one-quarter wavelength phase difference between the two modes at the output. As shown in Equation (1.31), this quadrature phase relationship, combined with equal amplitudes of the two modes, generates a circularly polarized wave. The eigenmode analysis allows for accurately determining the modal field distributions, enabling precise design and optimization of the polarizer to achieve the desired phase shift and polarization state.

Remark 2.3.1 [Dual polarization capability]. It is important to note that, concerning the diagonal symmetry of the polarizer, one of its eigenmodes is always antisymmetric. This implies that if exciting the square-waveguide-based polarizer with the TE₀₁ results in RHCP, the TE₁₀ must result in LHCP, or vice versa, depending on the choice of the transverse coordinates.

This principle can be visualized as decomposing the incident waveguide modes from Figures 2.2a and 2.2b into the orthogonal basis formed by polarizer eigenmodes depicted in Figures 2.3a and 2.3b. While the horizontal waveguide mode (Figure 2.2a) can be expressed as a positive sum of the two polarizer modes, the vertical waveguide mode (Figure 2.2b) requires the negative of the antisymmetric polarizer mode (Figure 2.3b). Moreover, assuming that the condition for circular polarization (1.31) is satisfied by the polarizer eigenmodes, taking their positive sum is equivalent to the plus sign option in Equation (1.32), hence RHCP. Conversely, the negative value of the antisymmetric mode represents the negative sign option, hence LHCP. Although this principle was illustrated using the square waveguide structure, the same holds for the circular geometry with its two orthogonal degenerate TE₁₁ modes (Figures 2.2c and 2.2d). This unique property enables the structures to produce dual circular polarization simply by switching between two excitations.

Furthermore, due to the mirror symmetry of both polarizers, optimizing the structure with respect to just a single orientation of circular polarization is sufficient. By the essence of the matter, the other polarization must retain the same performance parameters, as will be proven by simulation.

2.3.1 Figures of merit

A crucial outcome of the eigenmode analysis is the insight into the operational principles, which helps define relevant variables and performance parameters intrinsic to the structure's geometry, ultimately aiding in polarizer optimization. The optimiza-

tion process aims to produce circular polarization while minimizing production costs, primarily by reducing the polarizer length, L . This necessitates maximizing the *specific mode phase shift*, given by

$$\Delta k_L(f) = \frac{1}{L} \int_0^L [k_2 - k_1](z, f) dz, \quad (2.1)$$

where k_1 and k_2 are the propagation constants of the two polarizer modes, and z is the Cartesian coordinate aligned with the propagation direction. This quantity represents the average difference in propagation constants between the two modes along the polarizer,³ effectively quantifying the rate at which the phase difference between them accumulates as they propagate. However, Equation (2.1) addresses only one of the two conditions for circular polarization (1.31), the other being the requirement for equal mode amplitudes:

$$\left. \frac{E_2}{E_1} \right|_{z=L} = 1, \quad (2.2)$$

where E_1 and E_2 are the amplitudes of the two modes and the polarizer output. A weighted aggregate of Equations (2.1) and (2.2) forms the objective function of the optimization problem, with the variables being the geometric parameters of the polarizer cross-section. Intuitively, larger inserted shapes induce a greater phase lag per unit length but also introduce more considerable amplitude distortions between the modes. This displays an inherent conflict within the problem, necessitating a trade-off. From an application perspective, a balance must be struck between the length of the structure, which compensates for a lower phase delay per unit length, and polarization purity, which is compromised by unequal mode magnitudes.

2.3.2 Comparison of symmetric waveguides

To conclude the eigenmode analysis, a decision will be made, using the previously introduced figures of merit, regarding which geometry is better suited for polarization control, considering both practical and performance aspects. Ideally, a minimal frequency dependence of both figures, Equations (2.1) and (2.2), is desired. However, due to the inherently resonant operational principle of the waveguide, achieving feasible performance across an ultrawide band with a single section of such a polarizing structure is not considered possible.

Before proceeding, the practical evaluation of Equations (2.1) and (2.2) should be addressed. Given that both polarizers are analysed as uniform waveguides (Figures 2.1a and 2.1b), the propagation dispersion between the two modes, and consequently both metrics, can be approximated as constant throughout the polarizer, i.e., $\partial_z \Delta k_L = 0$. This approximation allows Equation (2.1) to be expressed as

$$\Delta k_L(f) = [k_2 - k_1](f), \quad (2.3)$$

and the overall mode phase shift at the polarizer output is given by

$$\Delta\phi(f) = L [k_2 - k_1](f). \quad (2.4)$$

³This quantity is analogous to the birefringence effect observed in optics, where a material exhibits different refractive indices for different polarizations, causing a phase difference to accumulate between them as they propagate. Here, the waveguide structure, due to its geometry, effectively creates different propagation constants for the two orthogonal modes, leading to a similar effect.

Furthermore, this simplification permits evaluating both Equations (2.2) and (2.3) from a single reading at the polarizer output. For this purpose, an *E-field probe* functionality within CST Studio Suite was utilized, allowing the magnitude and phase of the electric field to be determined at a specified point in space and evaluated across all frequencies. Consequently, the objective function for maximum specific phase shift, Equation (2.1), is transformed into the minimization of

$$L_{\perp}(f) = \frac{\pi}{4} \frac{L}{\Delta\phi(f)} \quad (2.5)$$

representing the polarizer length required to achieve a mode phase shift of $\pi/4$.⁴ This modified objective function can be readily computed using the *Template-Based Post-Processing* feature within CST Studio Suite, using $\Delta\phi(f)$ obtained from the *E-field* probe result. Moreover, the practical feasibility of the polarizer is inherently incorporated into this formulation.

The two polarizers depicted in Figures 2.1a and 2.1b are modelled with a similar cutoff frequency to facilitate a fair comparison. A diameter of 50 mm for the circular waveguide and a side length of 50 mm for the square waveguide are selected for the operating band of 4.7 GHz to 5.7 GHz. This selection results in a cutoff frequency of approximately 3 GHz for both underlying waveguides. As previously discussed, both polarizer metrics, Equations (2.2) and (2.5), are predominantly influenced by the cross-sectional geometry. Consequently, both polarizers have been parameterized by the width, w , of their chamfering inserts, as depicted in Figures 2.1a and 2.1b.

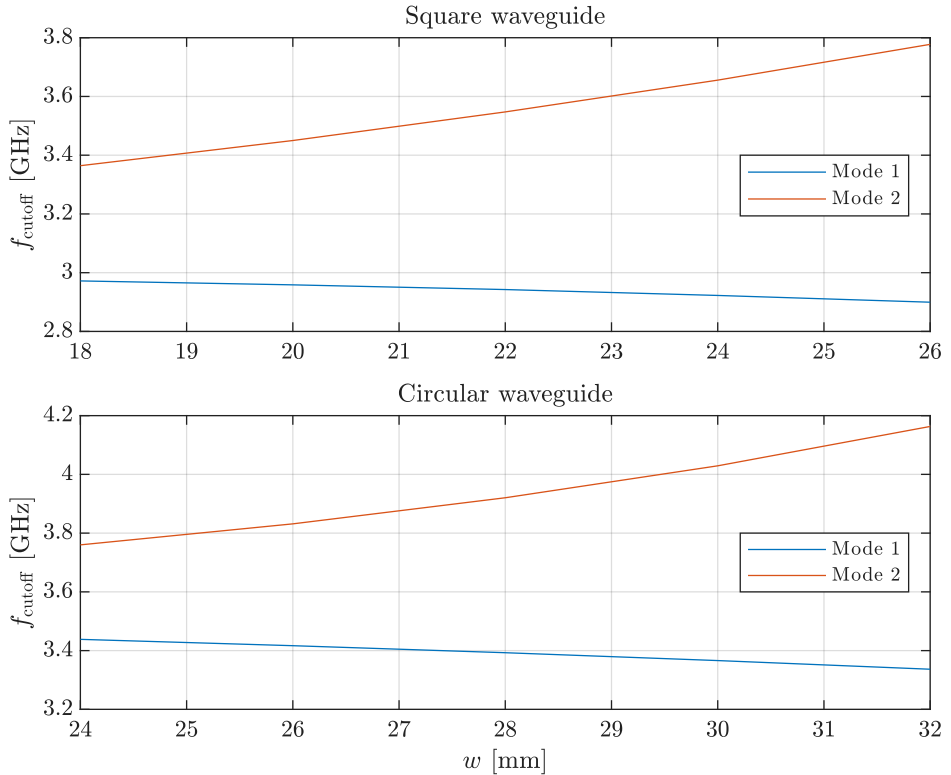


Figure 2.4: Polarizers: cutoff frequencies

⁴It is important to note that, due to phase wrapping, the cross-section tuning simulations must be conducted for a polarizer shorter than that required to produce a $\pi/4$ phase shift.

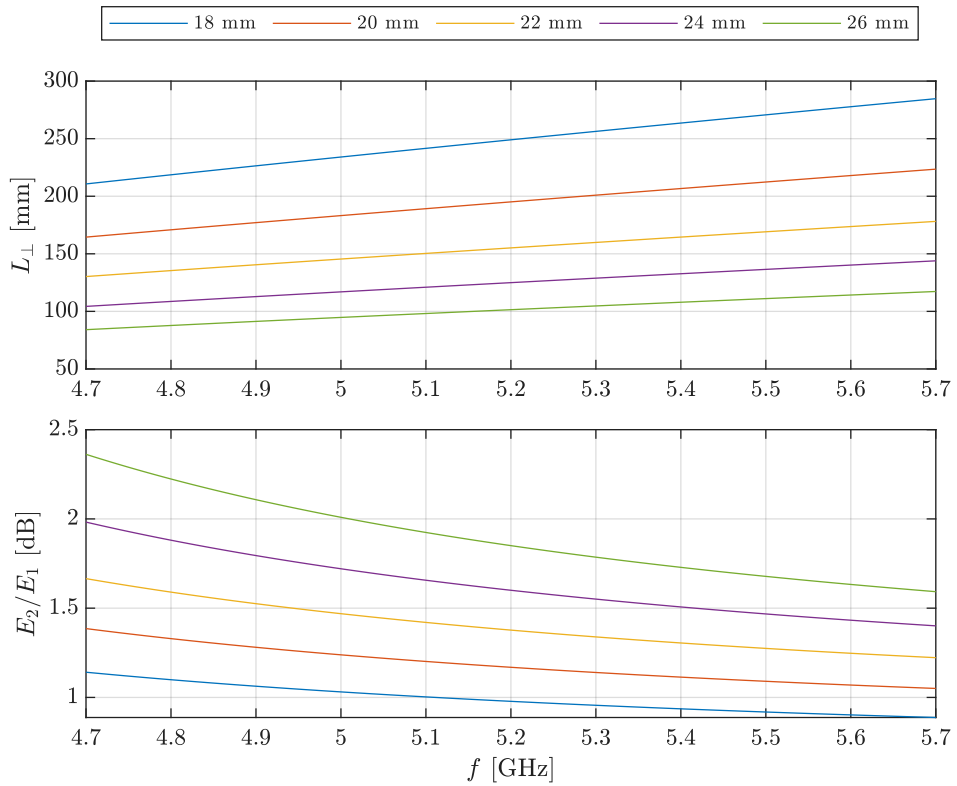


Figure 2.5: Square polarizer: cross-section tuning

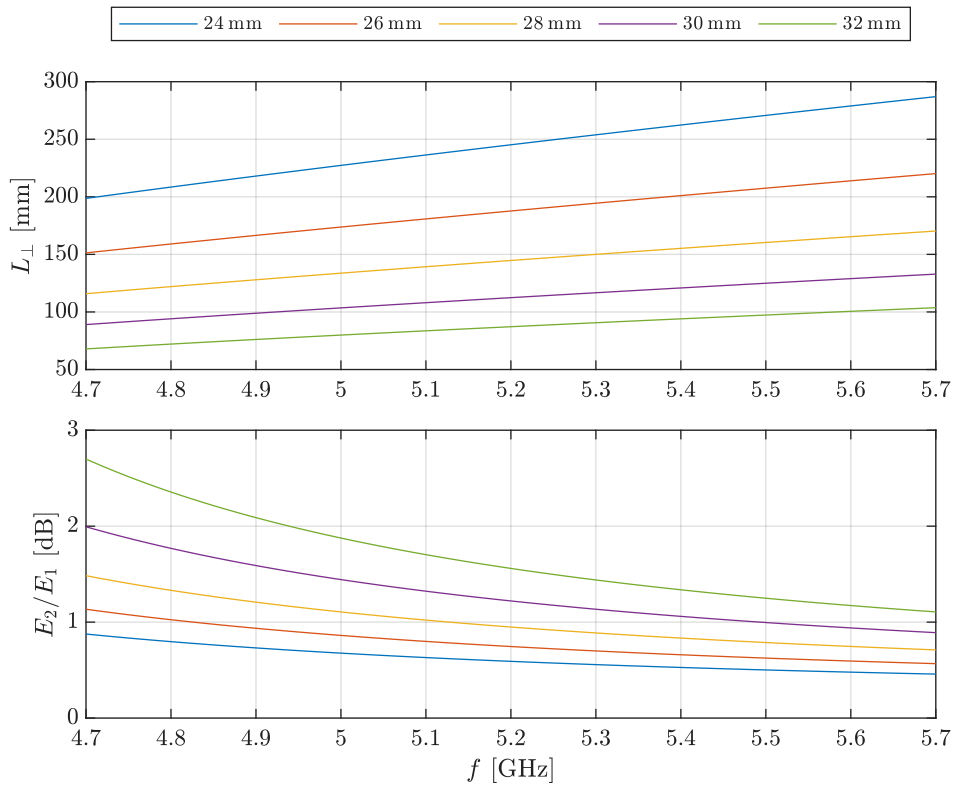


Figure 2.6: Circular polarizer: cross-section tuning

The mode cutoff frequency dispersion in Figure 2.4 is observed to be similar for both polarizers. However, a comparison of Figures 2.5 and 2.6 reveals that the square waveguide achieves superior phase dispersion while maintaining a lower amplitude dispersion gradient. Henceforth, this text concerns the design of a square waveguide polarizer, and the simple term *polarizer* will refer to this specific kind.

2.4 Square waveguide polarizer

With the fundamental waveguide structure established, the complete polarizer design can now be elaborated upon. This section outlines the design procedure, including all key considerations and design choices made. The process begins by defining the design requirements, which will serve as the foundation for modelling the structure.

Selection of parameters. The first step in the design process was to define the operating band. A frequency band spanning from 4.7 GHz to 5.7 GHz was selected for this polarizer. This range was chosen to cover common satellite communication and radar systems applications.

Based on this frequency range, the initial dimensions of the square waveguide were determined. As outlined in Section 2.3.2, the corresponding side length of 50 mm was selected for the square waveguide. This value was chosen based on the commercially available WR-187 rectangular waveguide,⁵ a standard component with dimensions and frequency range specified in [23]. However, it is essential to note that the insertion of prisms into the square waveguide, a key element of the design, significantly alters the dispersion characteristics compared to a standard rectangular waveguide. Thus, the 50 mm value was chosen as a starting point and further refined through simulations.

Subsequently, simulations were carried out to confirm the suitability of this dimension. The results of these simulations, which were already presented in Figure 2.4, show the cutoff frequencies of the waveguide with the inserted prisms. These cutoff frequencies are critical as they define the operating bandwidth of the waveguide. Based on the simulated cutoff frequencies, it was confirmed that the 50 mm side length provided an appropriate operating bandwidth for the target frequency range of 4.7 GHz to 5.7 GHz.

With the side length established, the next step involved determining the dimensions of the chamfering and the overall length of the polarizer. These parameters were determined through a parametric sweep using simulations. This involved systematically varying the chamfering width and observing its impact on the polarizer's performance. The results of this parametric sweep are presented in Figure 2.5.

After carefully analysing the simulated results, a chamfering width of 23 mm and a polarizer length of 126 mm were chosen. These values were selected to provide optimal performance with respect to polarization purity, meaning the ability to effectively transform a linearly polarized wave into a circularly polarized one. Additionally, these dimensions maintain a satisfactory axial ratio, which, as represented by the amplitude ratio in Equation (2.2), is a critical measure of the quality of the generated circular polarization.

⁵Also known as WG12 in the RCSC standard and R48 in the IEC standard.

2.4.1 Simulation results

The polarizer design section concludes with an evaluation of the polarizer's performance under full-wave simulation. Previous simulations were limited to analysing the eigenmode properties of the polarizer geometry. Consequently, it remains to be verified that the proposed solution functions as intended, i.e., that a linearly polarized TE₀₁ or TE₁₀ wave, guided by a square waveguide (as depicted in Figures 2.2a and 2.2b), is effectively converted into a circularly polarized wave upon excitation of the structure.

To simulate more realistic operating conditions, two sections of standard rectangular waveguide, with the same side length as the polarizer, are introduced at each end of the polarizer structure, as depicted in Figure 2.7. The input waveguide section facilitates the excitation of the polarizer with a linearly polarized wave. The output waveguide section serves as a rudimentary radiating element, allowing for an initial assessment of the radiated field. It also allows for verification that the generated circular wave maintains its integrity during the transition from the polarizer to a subsequent waveguide section while also minimizing the influence of reflections. This configuration further permits an examination of the radiation characteristics of the open-ended waveguide, providing preliminary insights into parameters such as co-polarization, cross-polarization directivity, and axial ratio, effectively representing a minimalist circularly polarized antenna.

The results, in the form of radiation patterns for co- and cross-polarizations of both incident waveguide modes, are presented in Figure 2.8. Other antenna parameters, such as scattering parameters, are not studied since the antenna in Figure 2.7 serves only as a validation of the polarizing functionality. While serving as a valid check of the radiation properties, the radiation from an open-ended waveguide suffers from large reflections due to the unmatched transition from a waveguide into free space. Perhaps the most crucial quality factor of circular polarization, the axial ratio, is evaluated in the far-field and is analogous to Equation (2.2), which describes the ratio of the orthogonal *E*-field components.

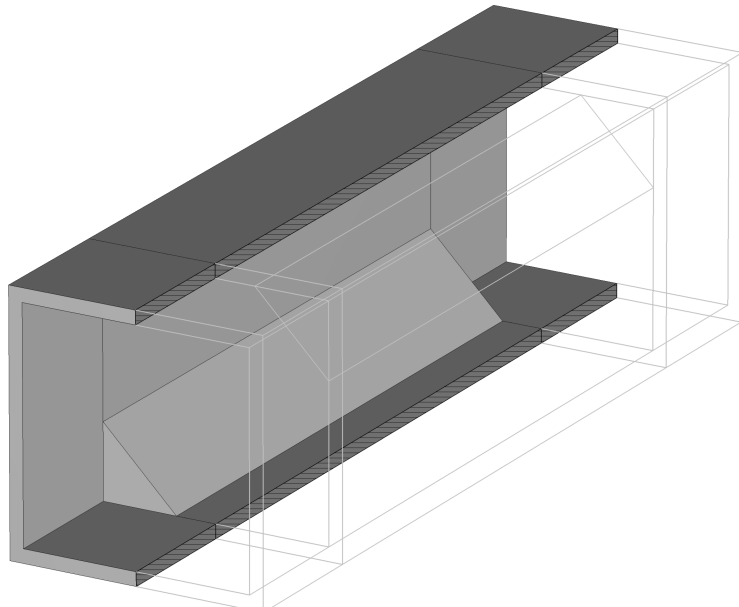


Figure 2.7: Final polarizer: model

These results confirm the previous eigenmode analysis. As shown in Figure 2.8, the axial ratio maintains a low value (with values below < 3 dB generally acceptable), even reaching 0 dB around the centre of the design band. The elevation radiation patterns are displayed at the centre frequency.

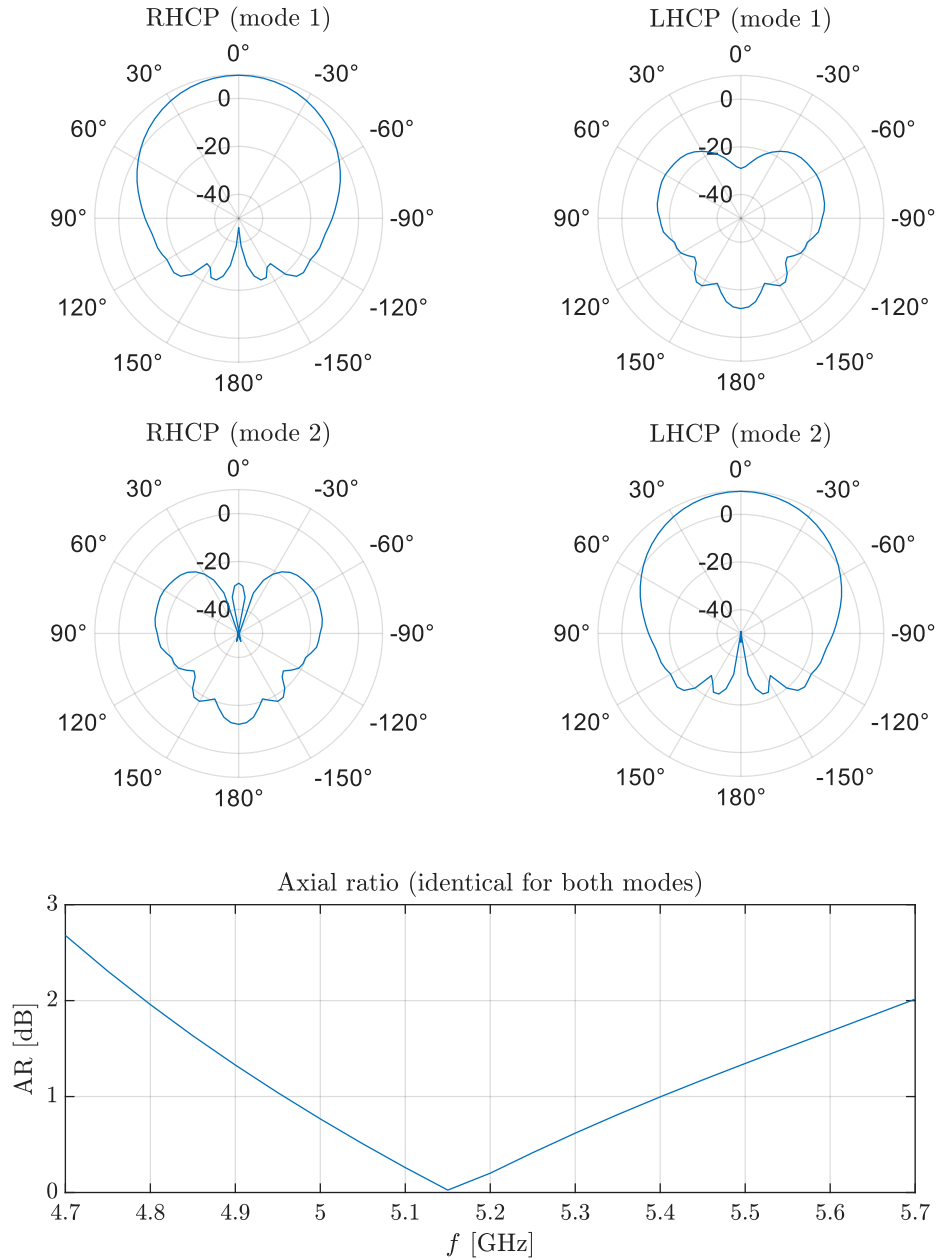


Figure 2.8: Final polarizer: radiation properties

Chapter 3

Feeding structure

This chapter details the design of a transition from two coaxial cables into a square waveguide, with each cable exciting only one of the fundamental TE_{01} and TE_{10} modes propagating within the waveguide. This facilitates an excitation of the polarizer, detailed in Chapter 2, equivalent to the artificial excitation used during the polarizer simulations, which were performed using a dual-mode waveguide port in CST Studio Suite.

The initial design considers the well-established problem of a single coaxial-to-waveguide transition employing a right-angled probe within the waveguide cavity. Following an evaluation of the single-feed adapter's performance, the feasibility of introducing a second feed into the same cavity is assessed, and the challenges posed by this are recognized. Separating the two excitation ports by a grating polarizer is adopted to allow their mutual displacement. This approach offers significant potential for reducing the mutual probe coupling below the margin of measurement error. Finally, simulation data are presented to demonstrate the performance of the final structure.

3.1 Coaxial-to-waveguide transition

The problem of coaxial-to-waveguide transition is well-established and rudimentary, with a vast body of existing research available, such as [24]. These transitions most frequently employ a *right-angle transition*¹ due to its ease of implementation and tuning, especially when compared to alternative solutions, such as the in-line transition described in [25]. This work adopts the most straightforward implementation, realized by a simple protrusion of the feeding cable's inner conductor through a side wall. The protruding conductor forms a radiating dipole element, exciting the waveguide with the carried wave. As with dipole antennas, this solution is expected to be relatively narrowband. Various methods exist to extend the bandwidth of low reflection, such as loading the dipole element with a metallic disc or cylinder or forming a conical widening at the probe's end. However, since the polarizer is already expected to operate in a limited band, such modifications are not considered in this thesis, trading the potential bandwidth benefits for enhanced ease of manufacturing.

The performance of a single right-angle transition, as illustrated in Figure 3.1,

¹While there is also the option to feed the waveguide *in-line*, i.e., by leading the coaxial cable's inner conductor through the adapter back wall, this technique is infeasible for the problem at hand. Apart from the obvious challenge of implementing this solution in a dual-feeding scheme, the in-line transition is known to generally perform in a narrower band, be prone to higher reflections, exhibit mode impurities in the waveguide, and pose a more difficult manufacturing challenge due to its use of a "shorting elbow" or other auxiliary constructions.

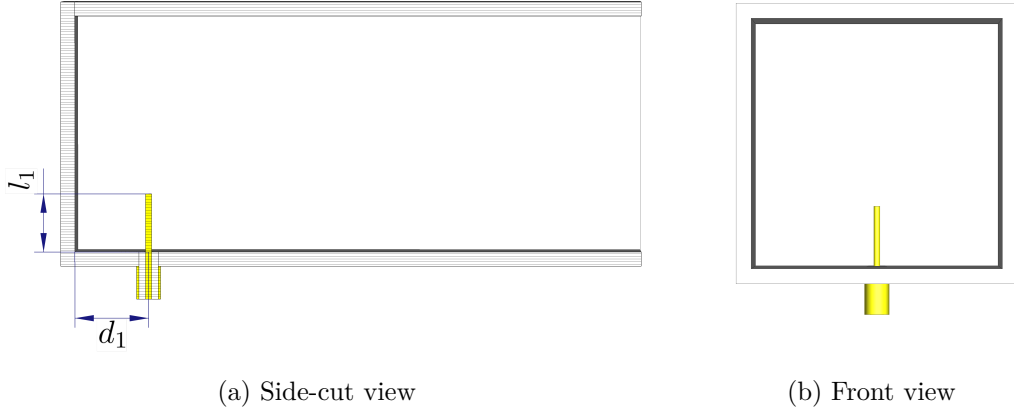


Figure 3.1: Single feed: section views

depends crucially on the precise tuning of two key parameters: the probe length, denoted by l_1 , and its distance from the “back-short”, denoted by d_1 . This section will focus on determining the optimal values of these parameters to achieve efficient power transfer within the dominant TE_{10} mode.

Design guidelines typically suggest a probe length of half the waveguide’s narrow dimension. Considering that rectangular waveguides are generally built with a 2 : 1 side length ratio,² the suggested probe length is given by

$$l_1 = \frac{3}{16} \lambda_c, \quad (3.1)$$

where λ_c is the centre wavelength. The probe acts similarly to a monopole antenna radiating into the waveguide. For optimal radiation, a monopole antenna’s length should be somewhat smaller than one-quarter of the operating wavelength due to the deviation from the idealized elementary dipole model, which assumes an infinitely thin conductor. Furthermore, the analogy is imperfect due to the presence of the waveguide walls and the influence of fringing capacitance at the probe tip. Consequently, the empirical value presented in Equation (3.1) aligns well with the theory of monopole antenna radiation as the working principle of the transition.

Since the monopole radiates omnidirectional the half-space above the waveguide wall, a significant portion of the input power is directed towards the back-short. Therefore, the distance to this shorting wall, d_1 , is primarily determined by the requirement for constructive interference of the wave reflected by the back-short with the waves emanating from the probe in the desired direction. To understand this, consider the wave propagation within the dominant TE_{10} mode. The back-short, acting as a conductive, hence a highly reflective wall, introduces a phase shift of π upon reflection. For constructive interference, the total phase shift experienced by the wave during its round-trip journey from the probe to the back-short and back to the probe must be an integer multiple of 2π . The simplest solution that satisfies the constructive interference requirement is to set the back-short distance to one-quarter of the guide wavelength.³

²The wider dimension A is typically chosen to be $3\lambda/4$ at the centre frequency as fundamental TE_{10} mode propagation is limited by the lower mode cutoff, occurring for $\lambda = 2A$, and the higher mode cutoff, for $\lambda = A$. Consequently, utilizing the 2 : 1 ratio, the narrow dimension is $3\lambda/8$.

³The relevant wavelength in this scenario is the guide wavelength, λ_g , which represents the wavelength of the propagating wave within the waveguide under the dominant TE_{10} mode. This is distinct from the free-space wavelength λ , as detailed in Example 1.2.7, and is given by Equation (1.53).

Consequently, the probe's distance to the back-short can be expressed as

$$d_1 = \frac{\lambda_g}{4} = \frac{\lambda}{4\sqrt{1 - \left(\frac{\lambda}{\lambda_{mn}}\right)^2}}, \quad (3.2)$$

where the cutoff wavelength λ_{mn} , corresponding to the cutoff frequency from Equation (1.52), can be simplified as $2A$, where A is the waveguide side length.

Remark 3.1.1. While constructive interference theoretically occurs for any probe distance $d_1 = (2\nu + 1)\pi$, where $\nu \in \mathbb{N}_0$ (i.e., any odd-integer multiple of π), the quality factor of such resonances rapidly increases with distance, thus resonant wavelength. Consequently, higher-order resonances ($\nu > 0$) exhibit impractically narrow bandwidths and are highly sensitive to dimensional variations, such as engineering tolerances during fabrication, making them unsuitable for reliable operation. Therefore, the fundamental resonance ($\nu = 0$) is preferred for practical right-angle transition designs.

Single feed tuning. This section concludes with the optimization of the single-port adapter parameters. Unlike the polarizer tuning, design guidelines are now available, providing reasonable initial estimates. In conjunction with well-defined objective functions, these values are utilized as the starting point for a multi-variable optimization. The primary objective is efficient energy transfer from the coaxial TEM mode to one of the fundamental waveguide modes (TE₀₁ or TE₁₀); therefore, the optimization goal is defined as the minimization of port reflection (S_{11}).

Initial values for d_1 and l_1 , calculated from Equations (3.1) and (3.2), are 17.64 mm and 10.81 mm, respectively. Using these values, the optimizer minimizes S_{11} across the operating band, yielding optimized values of $d_1 = 15.62$ mm and $l_1 = 12.32$ mm. The corresponding performance is illustrated in Figure 3.2. The optimized values are in good agreement with the theoretical estimates, falling within an acceptable margin. The observed deviations are likely attributable to the excited waveguide's non-standard height.

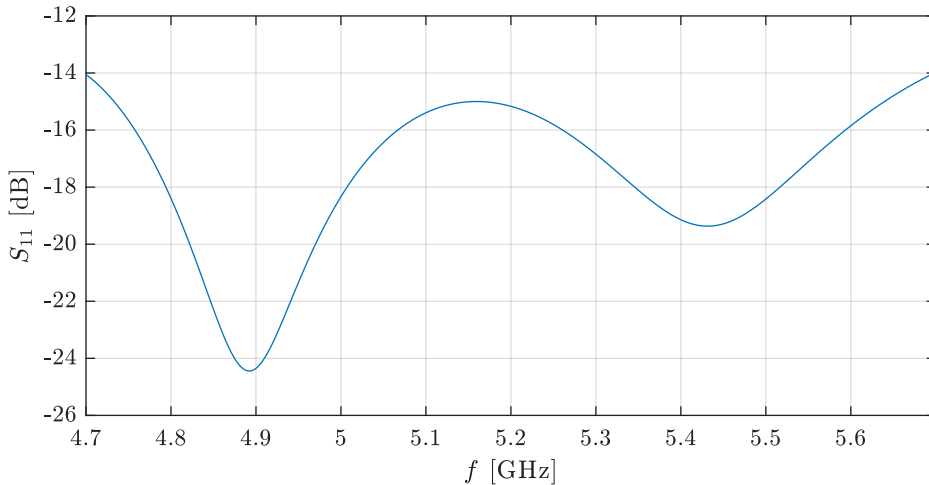


Figure 3.2: Single feed: reflection

3.2 Dual feed

The rudimentary feeding structure detailed in the preceding section served as an initial design step, facilitating the excitation of a single linearly polarized TE_{10} wave, which can subsequently be fed into the polarizer's input. This structure also provided a rough reference for the general parameters of a right-angle coaxial-to-waveguide transition. However, the polarizer detailed in Chapter 2 was designed to support transforming the other fundamental mode, the TE_{01} wave, into a circularly polarized wave of the opposite handedness. A dual feeding structure is required to leverage this capability, incorporating two ports positioned perpendicularly to excite each mode without excessive mixing or coupling. The design principles established in Section 3.1 are used as a foundation for this dual-feeding structure.

The design of a dual-feeding structure presents significant challenges, necessitating careful consideration of several key factors. A simplistic approach, placing both ports within the same plane ($z = d_1$), would likely result in high cross-talk due to electromagnetic coupling between the probes. Increasing the distance between the ports requires modifying either the length of one probe or its distance from the back-short. However, as determined in Section 3.1, such modifications significantly degrade individual port performance. An alternative, as mentioned in Remark 3.1.1, involves displacing one of the ports half a guide wavelength in the propagation direction. While this results in higher-order constructive resonance, it concurrently limits the operational bandwidth of the antenna.

A novel approach, introduced in [26], utilizes a *grating polarizer* to facilitate feeding probe displacement. This method theoretically enables arbitrary probe displacement without significantly degrading the performance of either port. As illustrated in Figure 3.3, the concept introduces a grating made of wires aligned parallel with the displaced port (Port 2). Due to its orientation, the grating is designed to discriminate the horizontally polarized waves radiated from Port 2, acting as a reflecting wall, while remaining transparent to vertically polarized waves, oscillating orthogonal to the wires, incident from the non-displaced port (Port 1).

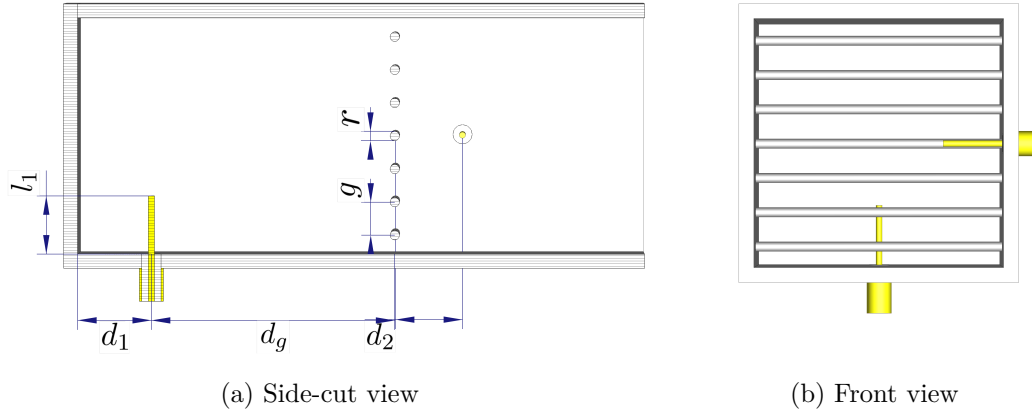


Figure 3.3: Dual feed: section views

Optimizing the proposed structure is considerably more complex. However, analysing the anticipated impact of individual parameters can improve initial estimates or eliminate them from the final optimization. For instance, the port parameters (probe length and distance from the back-short) can be assumed to primarily influence the reflection from the corresponding port without significantly affecting the other. Similarly, the distance, d_g , between Port 1 and the grating polarizer is assumed to have a negligible

impact on reflection from Port 2 (S_{22}). Finally, the grating geometry parameters, g and r (intuitively representing “grating density”), must be optimized with respect to both ports. As shown in [26], careful selection of these parameters is crucial to managing the trade-off between reflection from Port 1 (S_{11}) and port cross-talk (S_{21}), whereby a lower grating density reduces S_{11} at the expense of increased S_{21} , and vice versa.

3.2.1 Grating

As hinted above, a strategic approach is taken whereby certain variables are selectively eliminated to streamline the optimization process. After adding a grating to Port 1, the impact of the grating distance d_g on S_{11} can be analysed and optimized, as d_g is expected to have a negligible effect on S_{22} . While ideally, the grating should be transparent to Port 1 excitation and exhibit minimal influence on S_{11} , this is an oversimplification. Although not detrimental to the overall concept, the grating’s placement necessitates careful consideration.

Despite the generally low reflected energy from the grating, its introduction results in resonant behaviour in S_{11} , causing sharp increases in reflection at specific frequencies. As shown in Figure 3.4, the resonant wavelength is directly proportional to d_g . Full-wave simulation at the resonant frequency reveals that the grating and back-short form a resonant cavity, but only when the reflection from the grating destructively interferes with the forward-propagating wave at the cavity’s midpoint. This point creates a node for a standing wave, forming a cavity mode depicted in Figure 3.5, likely resulting from a superposition of fundamental modes.

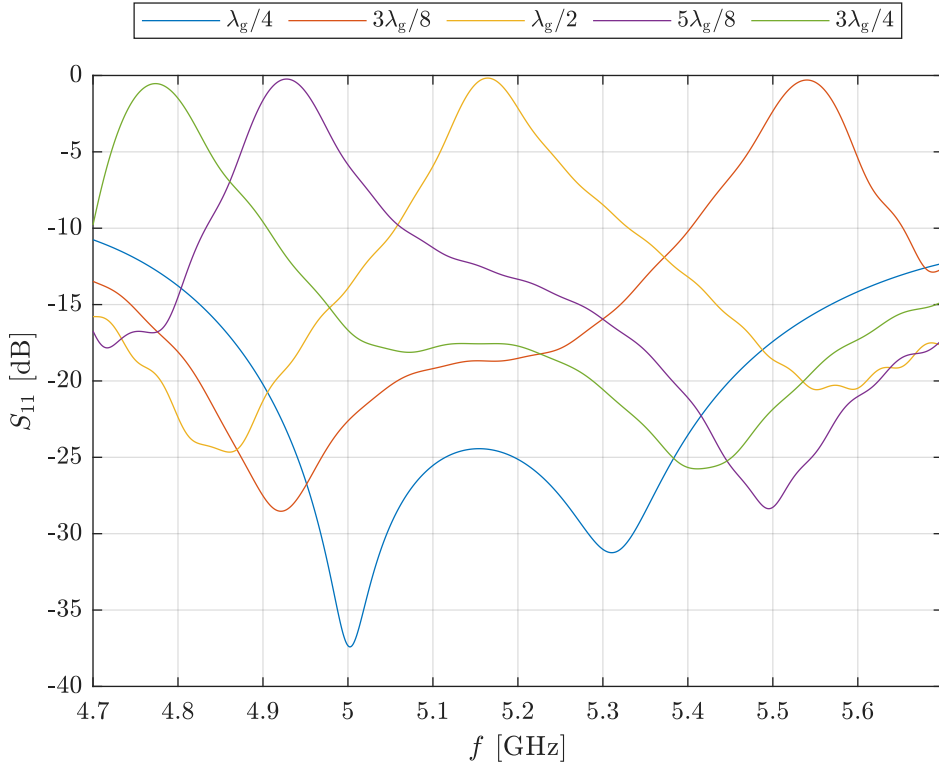


Figure 3.4: Single feed with grating: grating distance sweep

The results presented in Figure 3.4 are consistent with the tuning results reported in [26], where the authors identify recurring local minima in reflection at the centre

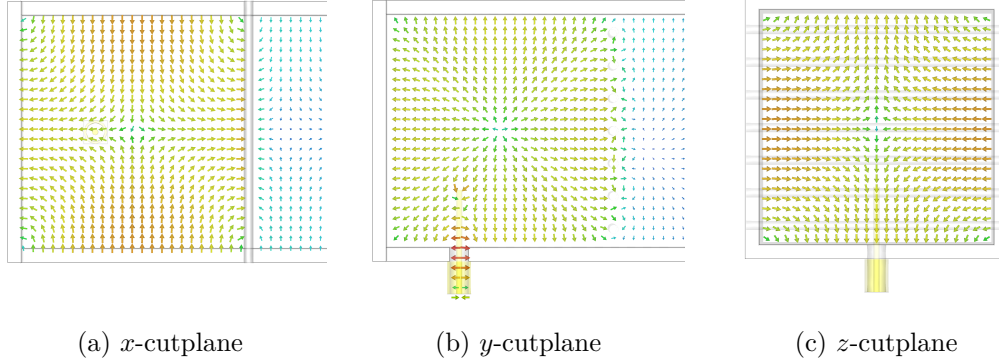


Figure 3.5: Cavity resonance: electric field section views

frequency for $d_g = \lambda_g/4$ and $d_g = 3\lambda_g/4$. In contrast, a local maximum is observed for $d_g = \lambda_g/2$. The referenced work further demonstrates that selecting $d_g = \lambda_g/4$ is suboptimal, as the port cross-talk continually diminishes with increasing d_g , eventually saturating around $d_g = \lambda_g/2$, provided that $d_2 \approx d_1$. Consequently, a potential optimal value is given by

$$d_g = \frac{3}{4}\lambda_g \quad (3.3)$$

Optimization. Passing the value given by Equation (3.3) as the initial estimate to the native optimizer in CST Studio Suite, the algorithm refines it to $d_g = 60.81$ mm with respect to the optimization goal to achieve $|S_{11}| < -15$ dB, evaluated as a sum of differences across the operating band. The resulting reflection performance is illustrated in Figure 3.6.

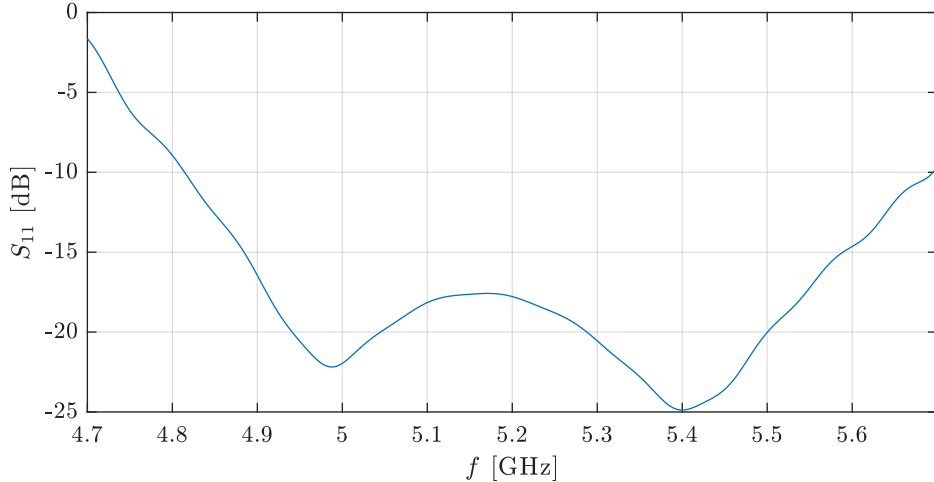


Figure 3.6: Single feed with grating: reflection

3.2.2 Second feed

The structure depicted in Figure 3.3 is completed with the introduction of the second port. This configuration defines a high-dimensional optimization problem, the solution of which is challenging due to the propensity of many optimization algorithms to converge to local minima of the objective function. Consequently, achieving a satisfactory result

without manual intervention is often hindered. The initial estimate for the optimization consists of the following parameters:

- port parameters, probe lengths l_1 and l_2 , and distances d_1 and d_2 , obtained from the results presented in Section 3.1;
- grating distance, d_g , obtained from the results presented in Section 3.2.1;
- grating density parameters, namely wire radius r and wire gap g , estimated based on the values reported in [26].

These initial values yield results that exhibit reasonable performance and primarily serve to verify the proposed solution. With the initial performance assessed and its validity as a solution to the design problem confirmed, further refinement is pursued through optimization.

The optimization of grating parameters r and g is constrained to prevent invalid geometrical configurations, such as wires intersecting each other or the waveguide walls. Unfortunately, the native optimization tool does not support the necessary interventions in the algorithm to enforce these constraints. This limitation was overcome by employing native Python libraries, enabling the development of a custom optimization routine. Details of the script facilitating this constrained optimization are further discussed in Appendix A.

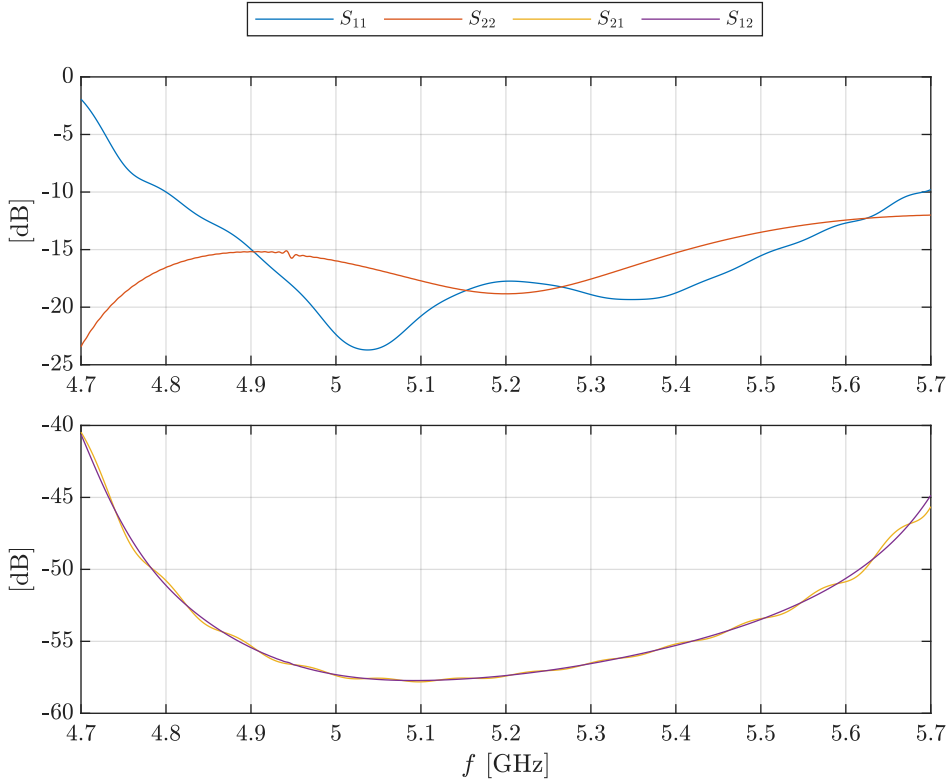


Figure 3.7: Dual feed: S-parameters

The final results of the optimization, presented as scattering parameters, are illustrated in Figure 3.7. Good performance is demonstrated across a relatively wide frequency band with both ports exhibiting low reflection (considering values below -10 dB acceptable) and cross-talk levels suppressed into values typically considered the noise

floor in most real-world measurements. The adjustments made to refine the initial performance were primarily related to the grating geometry, which did not perform adequately as a shorting wall for Port 2 in the initial estimate. Therefore, the grating depicted in Figure 3.3b was thickened by reducing the grating gap g and adequately increasing the wire count to 9. The optimum found for the dual feed parameters is

$$(d_1, l_1, d_g, d_2, l_2, r, g) = (15.62, 12.32, 60.81, 15.62, 12.32, 2, 5.2) \text{ mm}, \quad (3.4)$$

and the final model is depicted in Figure 3.8.

Remark 3.2.1 [Results commentary]. The ripple observed in Figure 3.7 at a frequency near 4.94 GHz is attributed to a cavity resonance. This resonance is caused by a small portion of energy penetrating the grating polarizer, as it is not an ideal shorting wall. At this frequency, the wavelength aligns with the distance $d_1 + d_g$, creating a resonant cavity between the back-short and the grating polarizer. In practice, this resonance is expected to diminish due to conductive losses. Its visibility in the simulation is due to the simulator being configured to terminate after a certain input energy level has diminished. At the same time, the resonance causes a portion of the energy to persist.

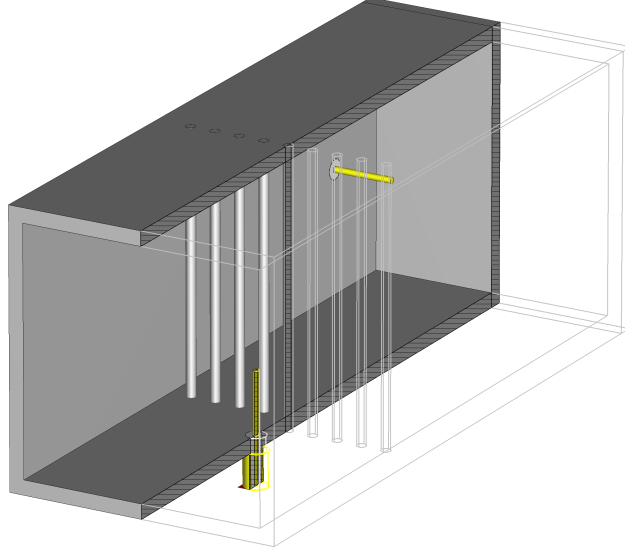


Figure 3.8: Final dual feed: model

Chapter 4

Antenna

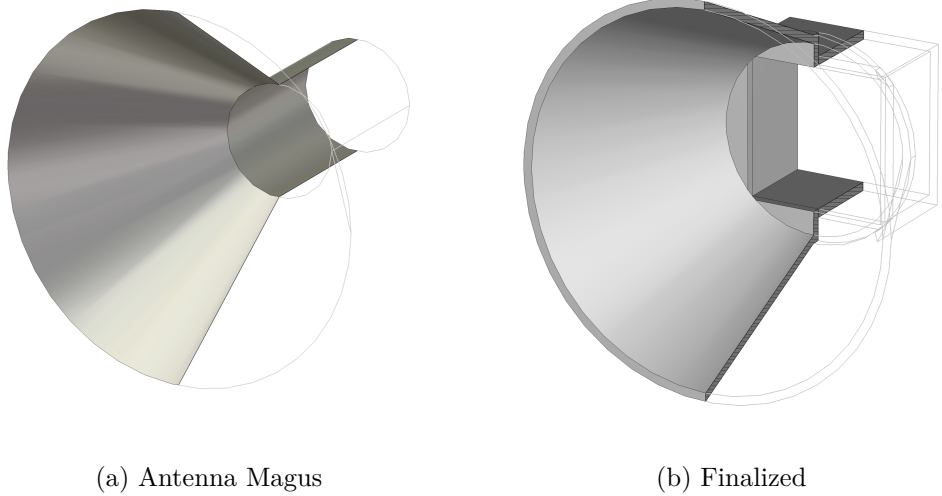
This chapter details the design of the third and final component of the system under consideration. As depicted in Figure 2.8, the polarizer demonstrates the potential for generating waves with favourable far-field radiation characteristics. However, to facilitate a smooth transition between the waveguide and free space, the structure must be coupled with an antenna exhibiting moderate gain, approximately 15 dBi. Furthermore, the antenna needs to support circular polarization. These requirements, particularly within the context of waveguide technology, suggest the utilization of a symmetrical antenna. While a pyramidal horn antenna with a square aperture could be inferred from the polarizer geometry, a conical horn antenna, adapted to the square polarizer outlet, is selected for this application due to its more straightforward fabrication process and robust support of circular polarization.

4.1 Conical horn

The radiation characteristics of conical horn antennas, including gain, aperture phase distributions, loss factors, and amplitude patterns, have been comprehensively re-examined in [27] utilizing spherical and quadratic aperture phase distributions. Moreover, a novel methodology for accurate computation of far-field amplitude patterns, including those in the far side and back lobe regions, was developed therein. This methodology leverages geometrical optics and diffraction theory, incorporating the Method of Equivalent Currents, which utilizes magnetic source quantities as discussed in Section 1.1.1.

The theoretical work presented in [27] and similar publications is anticipated to be integrated into the practical functionalities offered by Antenna Magus. This software facilitates the automatic synthesis of antenna designs, predicated on desired performance requirements, through neural networks. These networks are trained on an extensive database comprising existing antenna models and their corresponding performance data. Moreover, seamless integration with CST Studio Suite is supported, allowing for direct export of the synthesized antenna designs into the CST simulation environment for further analysis. An antenna model demonstrating this design approach, demanding the target gain of 15 dBi at the centre frequency of 5.2 GHz, is illustrated in Figure 4.1a.

The antenna depicted in Figure 4.1a provides a robust performance benchmark for subsequent adaptation into a rectangular waveguide configuration. Maintaining the original horn dimensions while modifying the feed from a circular to a rectangular waveguide is hypothesized to yield comparable results, contingent upon a smooth



(a) Antenna Magus

(b) Finalized

Figure 4.1: Conical horn: models

rectangular-to-conical transition that minimizes reflections detrimental to horn performance. Parametric sweeps of the horn flare diameter, D_f , and flare length, L_f , indicate that the target gain can be realized through various combinations of these parameters. Notably, for each value of flare length, the relationship between gain and flare diameter exhibits a concave function characterized by a distinct local maximum.¹ Consequently, selecting optimal parameters necessitates a trade-off between achieving the desired gain with a sufficient margin and minimizing the overall antenna dimensions. Two promising configurations were identified:

- (a) $D_f = 120$ mm, $L_f = 60$ mm, yielding a gain of 15 dBi,
- (b) $D_f = 130$ mm, $L_f = 70$ mm, yielding a gain of 15.5 dBi.

Ultimately, the latter configuration (b) was selected for the final design, prioritizing a gain margin despite the consequential increase in antenna dimensions. The finalized antenna design is depicted in Figure 4.1b. Its performance is benchmarked against an idealized Antenna Magus design, which assumes perfect electric conductors and zero wall thickness. As illustrated in Figure 4.2, adapting the model to a square waveguide configuration resulted in some deviations in the figures of merit. Nevertheless, the overall performance remains highly satisfactory, adhering to the required performance thresholds.

¹This behaviour is observed and examined in Figure 3 of [27].

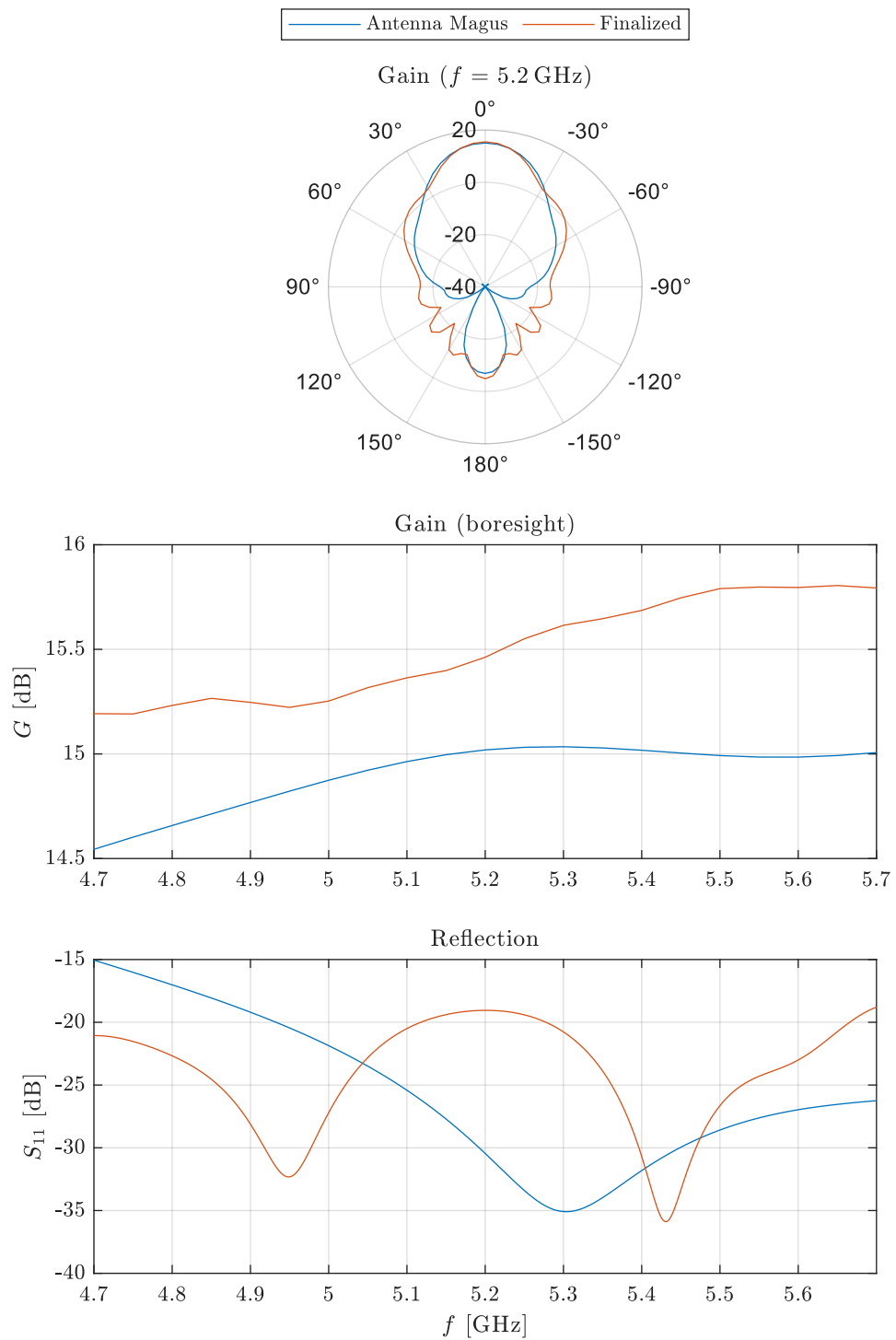


Figure 4.2: Conical horn: performance

Chapter 5

Final structure

This concluding chapter details the finalization of the antenna design, transitioning from individual component designs presented in Chapters 2 and 4 to a fully integrated and manufacturable product. The process begins with an assessment of initial full-system simulation results and an analysis of identified discrepancies. Driven by fabrication time constraints, a Minimum Viable Product (MVP) was developed, prioritizing core functionality. Subsequently, Design for Manufacturing (DFM) adjustments were incorporated into the structural design. The resulting DFM-compliant design was fabricated and characterized by Universal Microwave Technology, Inc, (UMT). The measured performance data is presented herein and compared against the simulated results, with a detailed discussion of the observed discrepancies.

5.1 Feed rework

Preliminary simulations indicate that the performance of the final structure deviates significantly from expectations, particularly concerning the operation of the dual-feeding mechanism. This discrepancy is primarily reflected in the S-parameters, as illustrated in Figure 5.1. While the performance of the feed incorporating a grating polarizer is acceptable in isolation, the figure also presents the S-parameters for a configuration with the grating entirely removed. This latter configuration represents the most straightforward implementation of a dual-feeding structure, previously discussed and dismissed in Section 3.2 due to inherent high cross-talk between ports. However, as demonstrated in Figure 5.1, despite exhibiting excellent individual performance, the grating polarizer provides only negligible improvement in cross-talk mitigation. This minimal benefit comes at the expense of a substantial increase in manufacturing complexity, overall size, and, consequently, the cost of the final product.

As previously addressed in Section 3.2, a manipulation of cross-talk levels can be achieved through increased grating density. Unfortunately, this tuning cannot improve the performance without significantly degrading port reflections. Consequently, integrating a grating polarizer fails to yield the anticipated performance improvements due to an as-yet-unidentified mechanism. A comprehensive investigation of this underlying mechanism necessitates further research, which falls outside this thesis's current scope and timeline, particularly considering the impending fabrication deadlines. Therefore, the MVP solution depicted in Figure 5.2 is adopted to expedite the development process. This design omits the grating polarizer and positions both ports within the same plane, ultimately proving an equally viable solution.

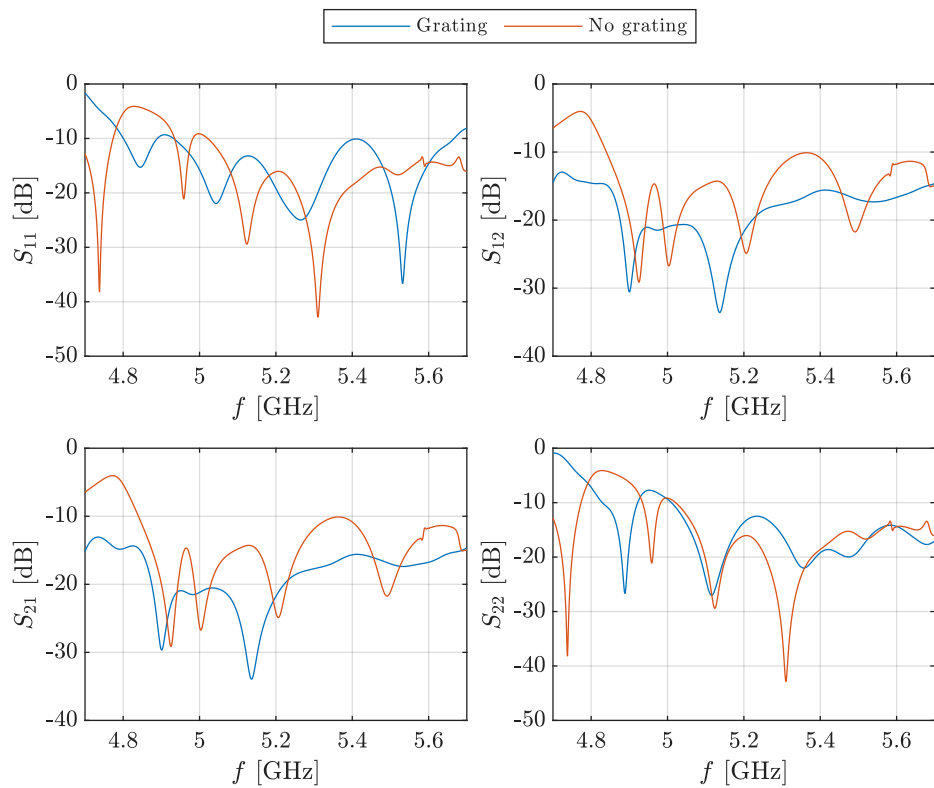


Figure 5.1: Final structure: grating performance

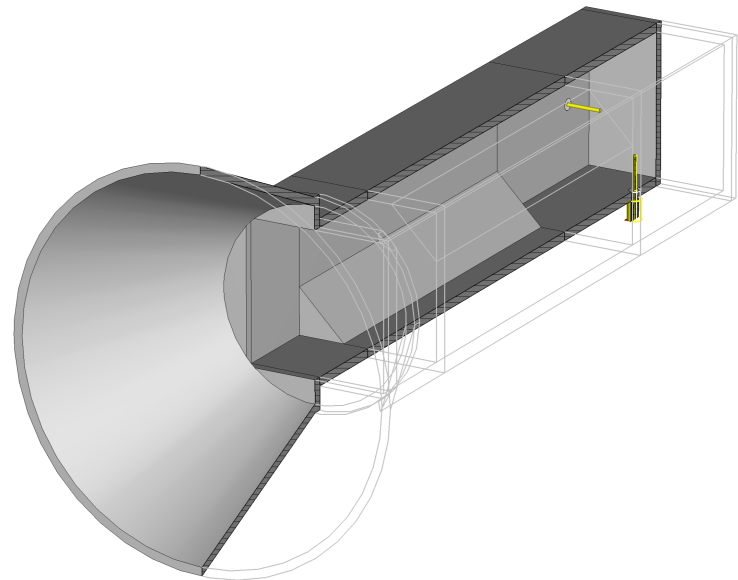


Figure 5.2: Final structure: MVP model

5.2 Product finalization

The structure illustrated in Figure 5.2 represents the finalized model used for electromagnetic simulations, establishing a benchmark for subsequent comparison with measurement data. These verification simulations employed exceptionally fine meshing settings and stringent convergence criteria based on energy dissipation to ensure the utmost accuracy. Concurrently, the final model underwent a design review with the principal engineer at UMT. This consultation led to the implementation of final DFM modifications. These adjustments, aimed at ensuring compatibility with standard CNC machining processes, involved modularizing the complete structure into five distinct components: the conical horn, square waveguide section, polarizer, dual-feed, and back-short. Each of these components was designed with standard waveguide flanges to facilitate assembly, and the antenna's geometry was further refined for efficient fabrication using drilling techniques. The resulting DFM-compliant model, depicted in Figure 5.3, demonstrates that the internal dimensions remain unchanged, thereby preserving the critical electromagnetic performance characteristics of the original design.

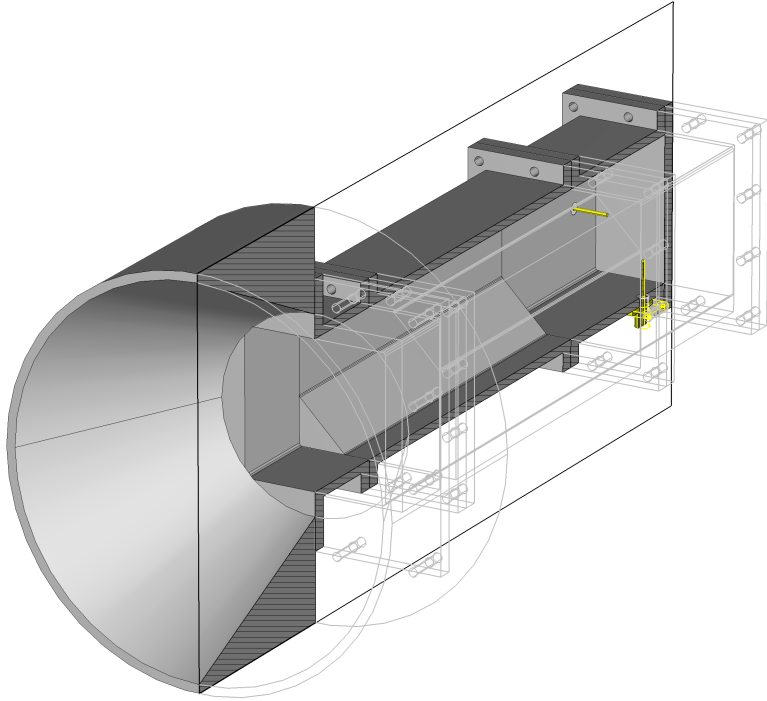


Figure 5.3: Final structure: DFM model

UMT, a leading company in the design, development, and manufacturing of custom components, antennas, and cables for microwave and millimetre-wave frequency bands, was selected as the fabrication partner for their state-of-the-art technology and proven expertise, which instilled high confidence that the product would be fabricated with minimal manufacturing tolerances. As anticipated, the measured network parameters of the fabricated antenna, presented in Figure 5.4, demonstrates excellent agreement with the high-fidelity simulations.

However, a considerable discrepancy is observed between the measured and simulated boresight gain, raising concerns regarding the accuracy of the radiation property measurements. Analysis of the anechoic chamber setup depicted in Figure B.1b suggests that the measurements may have been taken within the reactive near-field, potentially

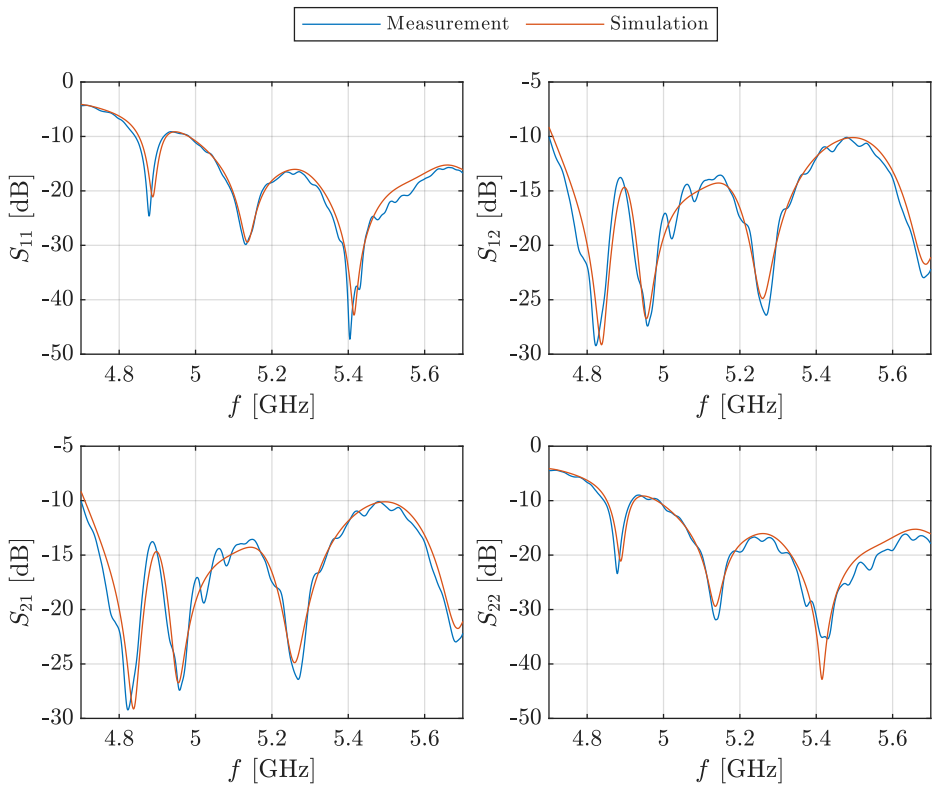


Figure 5.4: Measurement results: S-parameters

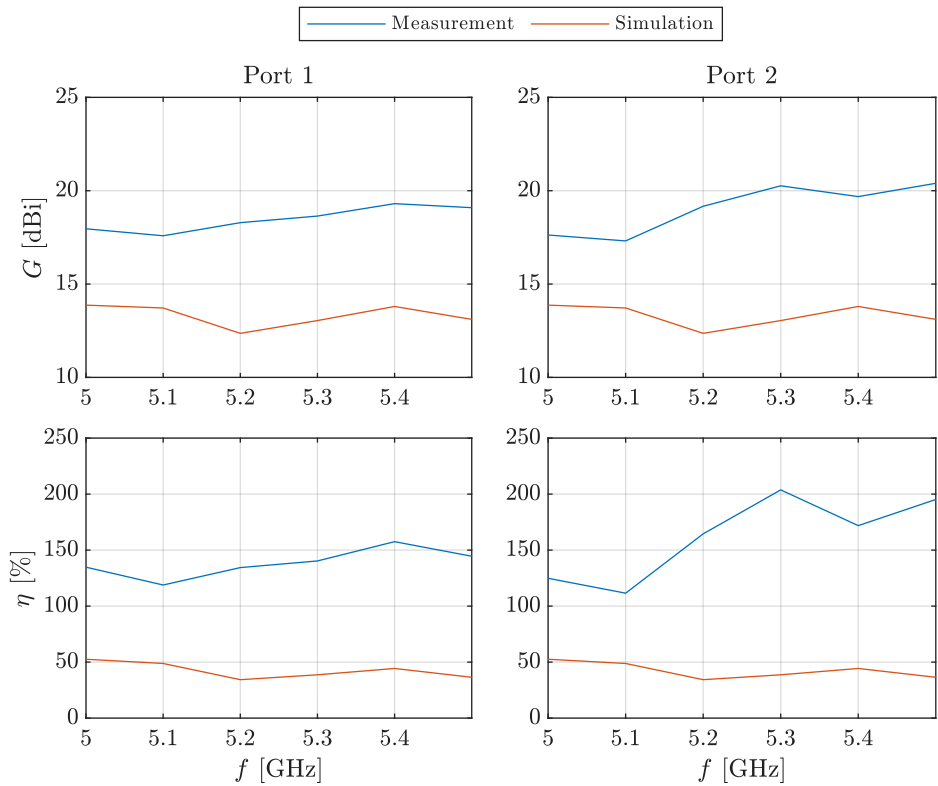


Figure 5.5: Measurement results: gain and aperture efficiency

violating the far-field criterion. This condition requires the antenna under test (AUT) to be positioned at a distance greater than the *Fraunhofer distance*, defined as

$$d_F = \frac{2D^2}{\lambda}, \quad (5.1)$$

where D represents the diameter of the AUT's aperture, was violated. The likelihood of a measurement error is further reinforced by examining the aperture efficiency

$$\eta = \frac{A_{\text{eff}}}{A_{\text{phys}}} = \frac{\lambda^2}{4\pi^2 R^2} G, \quad (5.2)$$

where A_{eff} and A_{phys} are the *effective* and *physical* aperture areas, respectively, G is the antenna gain, and $R = D/2$. Evaluating Equation (5.2) using the measured data and comparing it with the simulation results, as shown in Figure 5.5, reveals a clear inconsistency. The simulation data aligns with the expected aperture efficiency of approximately 50 %, a typical value for a simple conical antenna. Conversely, the measured data yield efficiency values exceeding the physically permissible limit of 100 %. However, these near-field effects appear to influence both polarization measurements equally. Consequently, they effectively cancel out during relative measurements, such as the axial ratio depicted in Figure 5.6 which exhibits excellent agreement with the simulation. The antenna parameters used during this discussion follow the usual definitions and can be found, e.g., in [28].

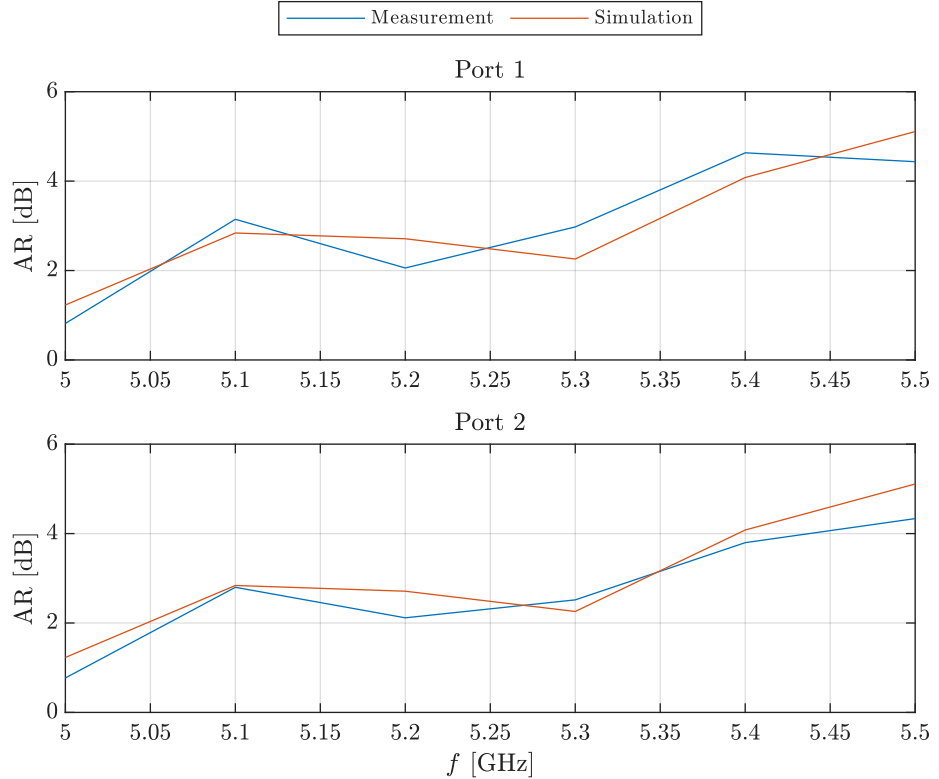


Figure 5.6: Measurement results: axial ratio

Figures 5.4 to 5.6 present a selected portion of the comprehensive measurement dataset, which is fully documented in Appendix B. This selective presentation was employed to maintain a focused discussion while ensuring a complete record of all acquired data readily accessible in the appendix. Specifically, the data showcased

in these figures correspond to Measurement 2 from the appendix. To ensure clarity in interpreting measurement data both in this section and the appendix, Figure 5.7 depicts the back view of the finalized antenna structure, designating Port 1 and Port 2, and establishing the orientation of the spherical coordinate system employed for all subsequent radiation pattern measurements.

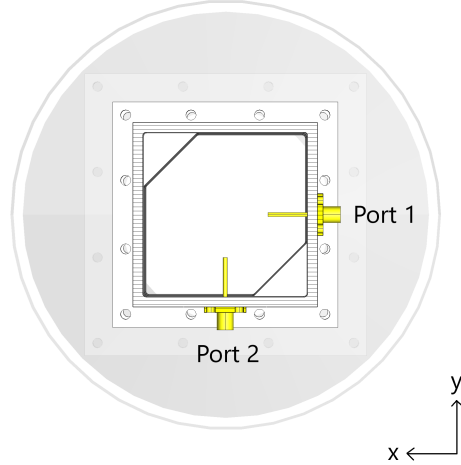


Figure 5.7: Back view of the final structure

Manufacturer's comment. AA discussion regarding the potential violation of the far-field distance threshold was held with the principal engineer at UMT, the company responsible for the product's fabrication and measurement. It was confirmed that the radiation properties were measured within the AUT's near field, specifically at a distance of

$$d = 23 \text{ cm} < 62 \text{ cm} \approx d_F \Big|_{5.5 \text{ GHz}}, \quad (5.3)$$

using an NSI-MI system employing the Near-Field Scanning (NFS) technique. NFS involves measuring the amplitude and phase of the electromagnetic field across a well-defined surface close to the AUT. Subsequently, these near-field measurements are mathematically transformed, typically using Fourier transforms or spherical wave expansions, to determine the far-field characteristics. While the NFS method is known for its precision, the complexity of the setup and data processing still makes it a potential source of the measurement error, as suggested by the unrealistic aperture efficiency values presented in Figure 5.5. Aside from potential calibration or field transformation errors, a hypothetical concern arises regarding the size of the probe used for NFS. As shown in Figure B.1b depicts, a relatively large open-ended rectangular waveguide was employed as the receiving probe, which could potentially introduce distortions into the measured near field.

Conclusion

The thesis presents a comprehensive study on the design, fabrication, and measurement of a novel dual circularly polarized antenna operating within the 4.7 GHz to 5.7 GHz frequency band. The work demonstrates high academic rigour and successfully achieves its core objectives, culminating in a functional prototype that exhibits excellent agreement between simulated and measured performance.

The primary academic goal of this thesis was to develop a waveguide-based antenna capable of producing switchable right-hand and left-hand circular polarization. This was achieved by introducing a novel polarizer design based on a square waveguide with chamfered corners, effectively creating a hexagonal waveguide structure. Through rigorous electromagnetic simulations and experimental validation, the thesis successfully demonstrates that this design allows for easy switching between polarization handedness by simply exciting one of the two orthogonal fundamental modes of the waveguide. This is a significant achievement with potential applications in polarization multiplexing, where dynamically controlling the polarization state can increase channel capacity. Moreover, the simple and robust design of the polarizer makes it suitable for scenarios where achieving polarization diversity might be challenging, such as in compact or integrated systems. The successful development of this novel polarizer constitutes the most significant academic contribution of this work, showcasing an innovative approach to polarization control in waveguide technology.

A further objective was to fabricate a physical prototype of the designed antenna and validate its performance through measurements. This goal was fully achieved, with the final product fabricated to high precision by Universal Microwave Technology, Inc. The measured performance demonstrates excellent agreement with the simulated results, strongly validating the design methodology and the accuracy of the electromagnetic simulations. The close agreement between simulation and measurement confirms the design's manufacturability, highlighting its potential for practical applications.

Despite the project's overall success, several potential areas for improvement are identified. The polarizer's performance could be enhanced by incorporating a tapered transition into the chamfered sections, potentially reducing reflections and improving the overall bandwidth, which warrants further investigation. Implementing multiple polarizer sections with varying geometries could also widen the operational bandwidth, albeit at the cost of increased complexity. Regarding the feeding structure, alternative coaxial-to-waveguide transition techniques, such as disc-loaded or prismatic probes, are known to widen the operation bandwidth. Finally, while the conical horn antenna provides satisfactory performance, considering a quad-ridge square pyramidal horn could offer a more robust and potentially broader bandwidth solution, especially for applications demanding higher polarization purity across a wider frequency range. These suggested improvements provide avenues for future research and development, building upon the solid foundation established by this thesis.

Appendix A

Constrained optimization

In advanced optimization scenarios requiring algorithmic manipulation, such as geometric adjustments after new parameter values are set, the native optimization tool within CST Studio Suite is insufficient. While a range of settings is provided, the configuration is confined to optimization methods and algorithm-specific parameters. The remaining functionality is integrated within the operational framework of CST Studio Suite, thereby precluding the definition of proper constraints apart from specifying a bounding interval for each variable.

However, the CST Studio Suite installation incorporates a collection of CST Python libraries, as documented in [29]. These libraries allow external control of a CST Studio Suite instance and access to a subset of its features via a Python programming interface. Fortunately, the available features provide the requisite components for the construction of an optimizer class, thus enabling the establishment of an interface between an external optimization algorithm and automated simulation processes.

Listing A.1: Optimizer class initialization

```
from cst.interface import DesignEnvironment
from cst.results import ProjectFile, ResultItem

class CSTOptimizer:

    def __init__(
        self,
        project_path: str,
        optimization_config: dict[str, Any],
        vba_path: Optional[str] = None,
    ):
        self.project_path = project_path
        if vba_path:
            with open(vba_path, "r") as vba_file:
                self.check_geometry = vba_file.read()
        else:
            self.check_geometry = None
        self.cst = DesignEnvironment().connect_to_any_or_new()
        self.project = self.cst.open_project(self.project_path)
        self.result_module = ProjectFile(
            self.project_path, allow_interactive=True
        ).get_3d()
```

The code snippet in Listing A.1 illustrates a segment of the class initialization method. During initialization, the class receives the path to the target project, an optimization configuration in a dictionary data structure that allows for optimization method customization, results processing logic, objective functions and others, and an optional path to a VBA script. This script, if provided, is executed within CST Studio Suite using its built-in BASIC interpreter during each optimization step after new parameter values are set. Beyond this, the complete initialization method defines various runtime variables for progress tracking and unpacks the optimization configuration dictionary into individual attributes to enhance runtime efficiency. These latter components are not central to the described core functionality and are omitted in the snippet.

The primary motivation behind developing a custom optimizer lies in the ability to tailor the *objective function*. This function is evaluated at each iteration of the optimization process, serving to quantify performance, termed the *objective value*, for a given set of parameters suggested by the optimization algorithm. Within the context of simulation software, this typically involves updating the model with new parameter values, executing a simulation, and assessing the objective value. Constraints can thus be enforced by integrating a geometry check and potential adjustments after the model's structure is updated with the new parameter values. An implementation of this strategy within the optimizer class, with minor details omitted for clarity, is presented in Listing A.2.

Listing A.2: Objective function

```
def objective_function(self, x: np.ndarray) -> float:
    # Update parameters
    update_parameters = "Sub Main()\n"
    current_step = {}
    for name, value in zip(self.variable_names, x.round(5)):
        update_parameters += (
            f"StoreParameter(\"{name}\", {value})\n"
        )
        current_step[name] = value
    update_parameters += (
        "RebuildOnParametricChange(True, False)\nEnd Sub\n"
    )
    self.project.schematic.execute_vba_code(
        update_parameters, timeout=None
    )
    # Execute geometry adjustment VBA script, if provided
    if self.check_geometry:
        self.project.schematic.execute_vba_code(
            self.check_geometry, timeout=None
        )
    # Run simulation
    try:
        self.project.modeler.run_solver()
        self.last_run_id += 1
    finally:
        self.project.save(include_results=True)
    # Evaluate objective value
    return self.evaluate_step(current_step)
```

For improved clarity and logical flow, the processing of simulation results is encapsulated within a dedicated method. This modular approach is beneficial due to the organization of CST Python libraries into multiple modules. As illustrated in Listing A.1, the implementation utilizes the following two modules:

- `cst.interface` provides classes that facilitate the interface for controlling CST Studio Suite.
- `cst.results` enables read-only access to one-dimensional results stored in CST project files.

As shown in Listing A.2, the main body of the objective function concludes with a completed simulation, followed by saving the project to ensure the project files' accessibility to the result module. Subsequently, these results are processed and evaluated using the function detailed in Listing A.3. For brevity, the function evaluates the results using the *Sum of Differences* norm. The full implementation allows for choosing the goal norm via the optimization configuration dictionary.

Listing A.3: Optimization step evaluation

```
def evaluate_step(self, current_step: dict[str, Any]) -> float:
    # Get results
    results = [
        self.parse_results(
            self.result_module.get_result_item(
                treepath=goal["result"],
                run_id=self.last_run_id,
            ),
        )
    ]
    for goal in self.goals
    ]
    # Compute objective value
    objective_value = 0
    for result, goal in zip(results, self.goals):
        average_difference = sum(
            result - goal["target"]
        ) / len(result)
        objective_value += goal["weight"] * average_difference
    return objective_value
```

In addition to the core optimization routines, the optimizer class incorporates ancillary methods, as shown in the presented listings. While these utilities play an essential role, they are not the primary focus of this discussion. Among the utilities used in the listings are `get_constraints` and `get_options`, used in Listing A.4 and responsible for retrieving arguments relevant to the optimization method, and `parse_results`, tasked with preparing raw data from CST.

The foundational elements established thus far—simulation control, data retrieval, and performance evaluation—facilitate the integration of established optimization methods. Such methods are commonly found in data-oriented programming languages, with a particularly robust and widely recognized implementation available in the *SciPy* library, an open-source scientific computing library for Python thoroughly documented in [3].

Listing A.4: Use of CSTOptimizer with SciPy

```
from scipy.optimize import minimize

result = minimize(
    optimizer.objective_function,
    x0=np.array(optimizer.initial_values),
    method=optimizer.method,
    bounds=optimizer.bounds,
    constraints=optimizer.get_constraints(),
    options=optimizer.get_options(),
)
```

Listing A.4 assembles the complete logic, integrating all previously described components to enable an entire optimization process. While some supplementary logic concerning algorithm termination and the saving of optimal parameters is omitted here for brevity, all essential elements are present.

The VBA script for geometry validation and potential adjustments, executed within CST Studio Suite following parametric modifications, as outlined in Listing A.2, represents the primary advantage of this approach. This entire side project originated as a solution to the problematic optimization behaviour described in Section 3.2.2. Therefore, the VBA script designed explicitly for adjusting the grating within a dual-feeding structure for a square waveguide is presented in Listing A.5. This script serves both as a practical use case for the developed optimizer class and as a direct solution to the issue identified in the main body of this work.

Listing A.5: Grating adjustment script

```
waveguideSide = GetParameter("waveguideSide")
gratingGap = GetParameter("gratingGap")
wireDiameter = GetParameter("wireDiameter")
wireCount = GetParameter("wireCount")
Do While isGratingTooNarrow( _
    waveguideSide, gratingGap, _
    wireDiameter, wireCount)
    wireCount = wireCount + 2
Loop
Do While isIntersecting( _
    waveguideSide, gratingGap, _
    wireDiameter, wireCount)
    wireCount = wireCount - 2
If wireCount < 1 Then
    Err.Raise vbObjectError + 100, _
        "Main", _
        "No feasible grating geometry found."
    Exit Sub
End If
Loop
If wireCount <> GetParameter("wireCount") Then
    StoreParameter "wireCount", wireCount
    Call RebuildOnParametricChange(True, False)
End If
```

Listing A.5 again represents a segment of a larger code base, omitting rudimentary steps like variable definitions and error handling for brevity. The script utilizes three custom functions. Two of these functions perform geometric validity checks related to two cases of invalid grating arrangements with varying gaps:

- (a) A gap that is too narrow, resulting in a gap between the grating and waveguide walls.
- (b) A gap that is too wide, resulting in wires intersecting with the waveguide walls.

The functions detailed in Listing A.6 and Listing A.7 detect these two cases, respectively. They are corrected in the main program loop by adding or removing grating wires as needed.

Listing A.6: Check for a gap around the grating

```
Private Function isGratingTooNarrow( __
    waveguideSide As Double, __
    gratingGap As Double, __
    wireDiameter As Double, __
    wireCount As Integer __
) As Boolean
    gapAroundGrating = (waveguideSide - __
        wireCount * gratingGap - __
        wireDiameter) / 2
    If gapAroundGrating > gratingGap Then
        isGratingTooNarrow = True
    Else
        isGratingTooNarrow = False
    End If
End Function
```

Listing A.7: Check for intersection with waveguide walls

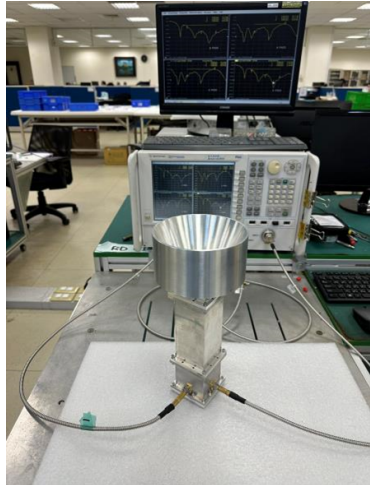
```
Private Function isIntersecting( __
    waveguideSide As Double, __
    gratingGap As Double, __
    wireDiameter As Double, __
    wireCount As Integer __
) As Boolean
    gratingEdge = (wireCount - 1) / 2 * __
        gratingGap + wireDiameter / 2
    If gratingEdge > waveguideSide / 2 Then
        isIntersecting = True
    Else
        isIntersecting = False
    End If
End Function
```

Appendix B

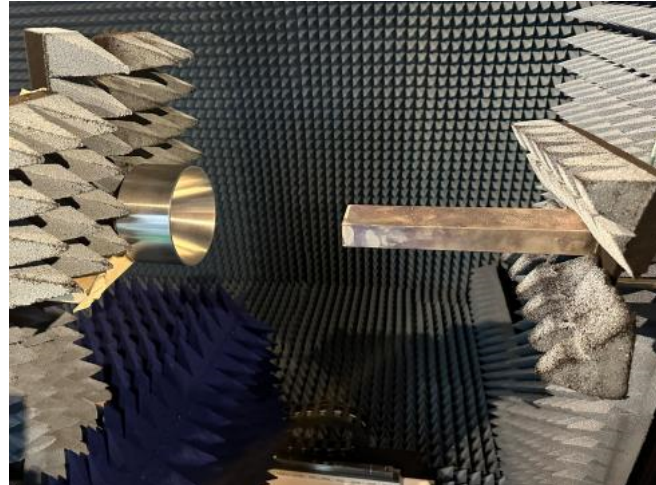
Measurement results

This appendix details the comprehensive measurement data for the antenna prototype, acquired across two campaigns by UMT whose contribution is gratefully acknowledged. Key results are presented within the main body of the thesis for comparison with simulations, while this appendix serves as a complete repository of all measured parameters.

The data presented includes S-parameters measured using an Agilent VNA, providing insights into impedance matching and power transmission across the operational frequency band. Furthermore, frequency responses of boresight gain and axial ratio are included. These parameters were measured in an in-house anechoic chamber using an open-ended waveguide as a sensing antenna. Radiation patterns, presented in the form of both elevation and azimuth cuts, were recorded at frequencies 5 GHz, 5.3 GHz, and 5.5 GHz. Both measurement setups are illustrated in Figure B.1.



(a) S-parameters



(b) Radiation properties

Figure B.1: Measurement setup

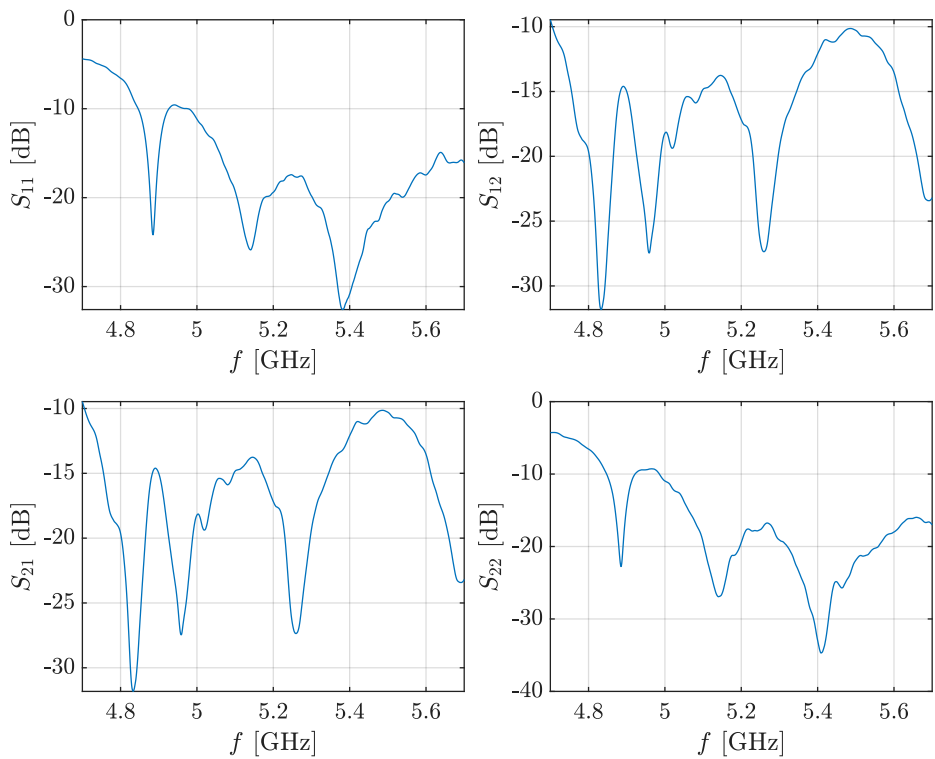


Figure B.2: Measurement 1: S-parameters

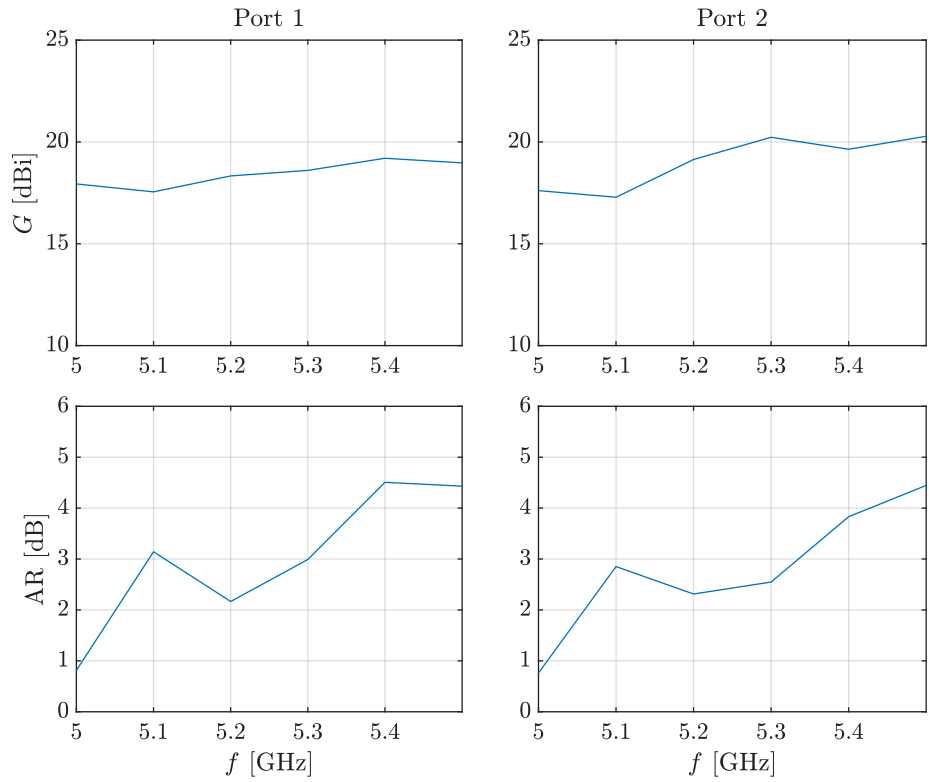


Figure B.3: Measurement 1: gain and axial ratio

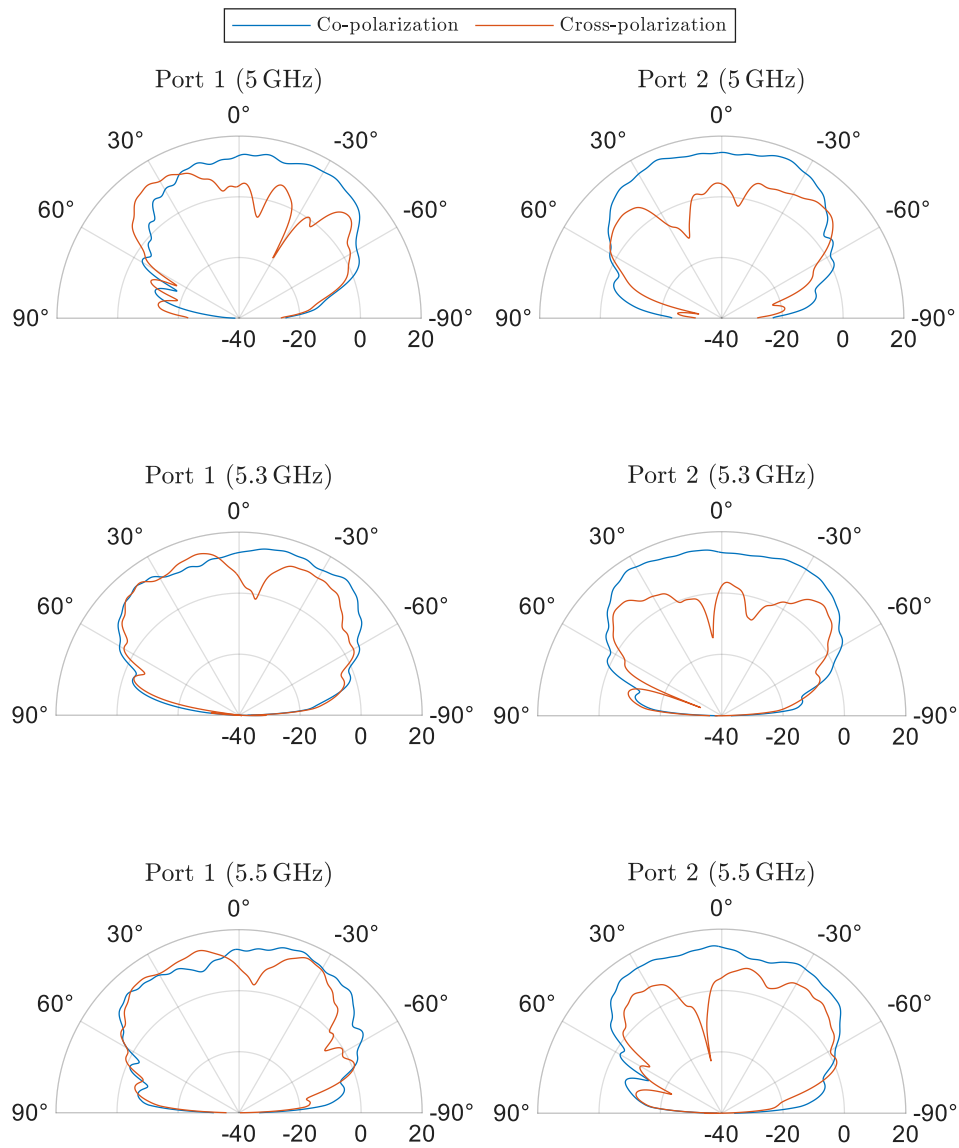


Figure B.4: Measurement 1: elevation radiation pattern ($\varphi = 90^\circ$)

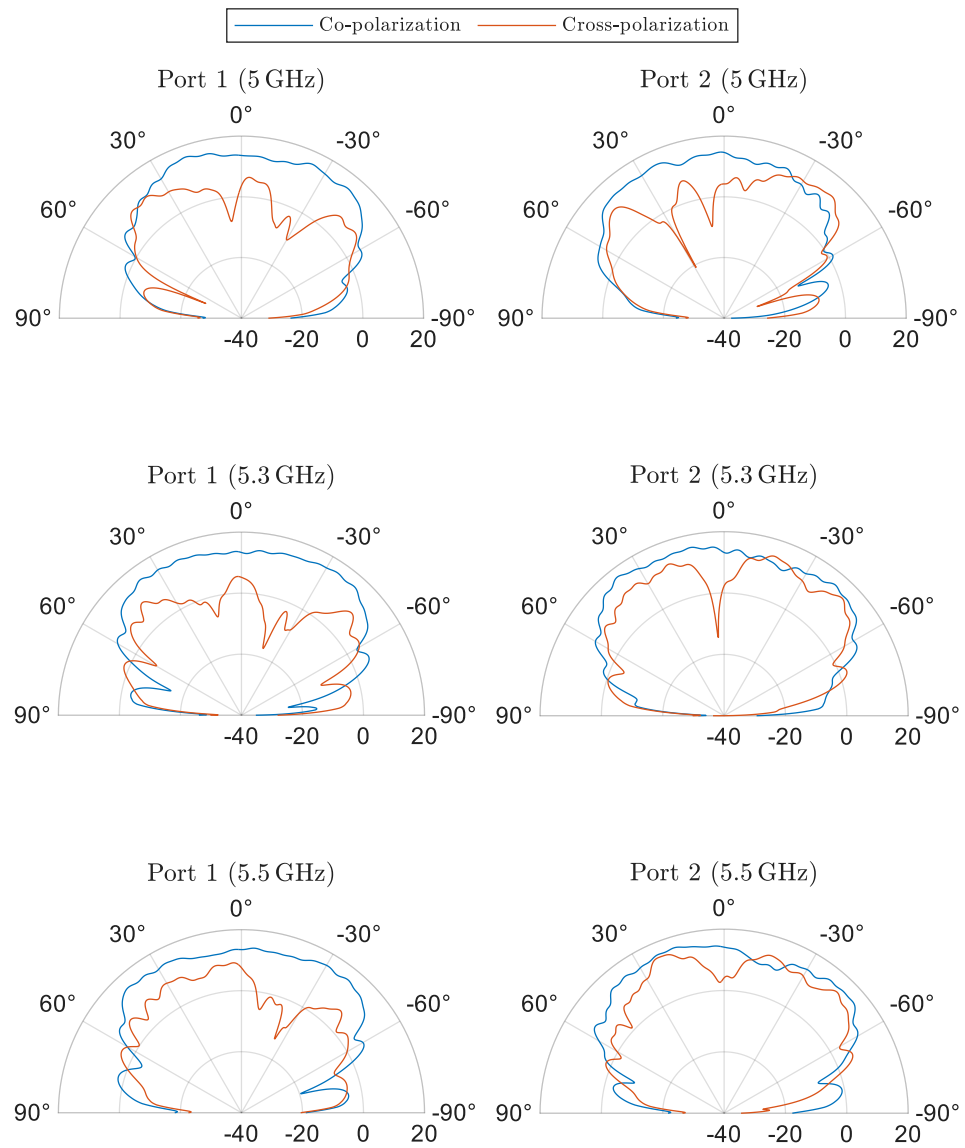


Figure B.5: Measurement 1: azimuth radiation pattern ($\varphi = 0^\circ$)

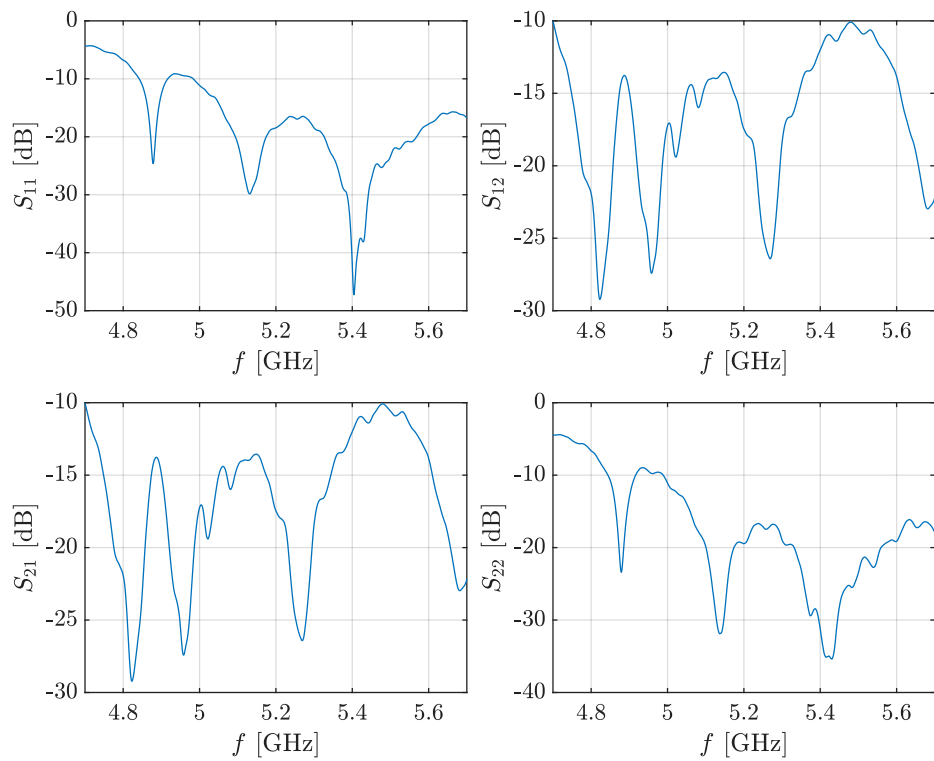


Figure B.6: Measurement 2: S-parameters

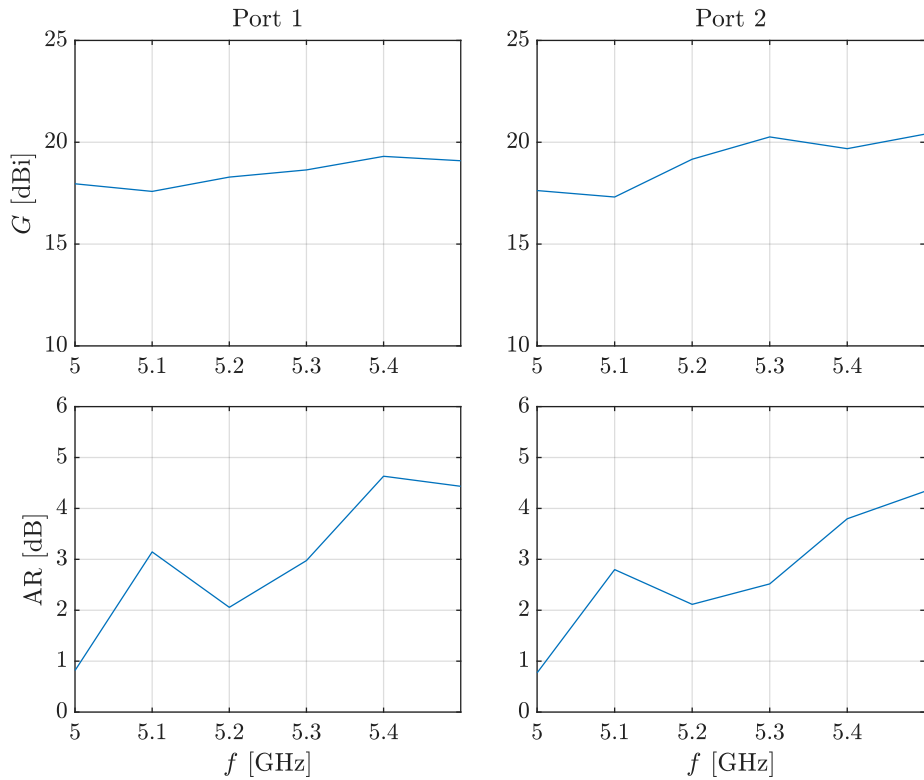


Figure B.7: Measurement 2: gain and axial ratio

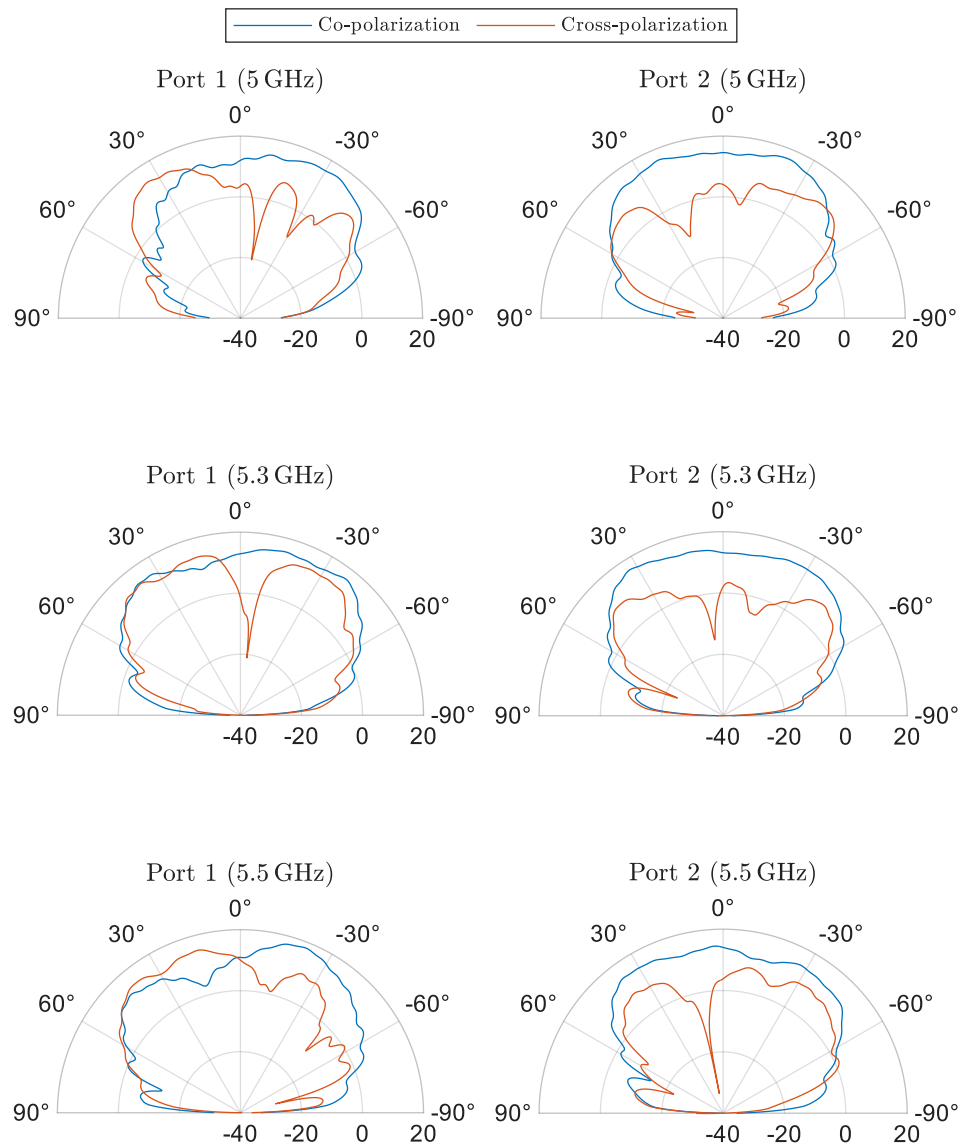


Figure B.8: Measurement 2: elevation radiation pattern ($\varphi = 90^\circ$)

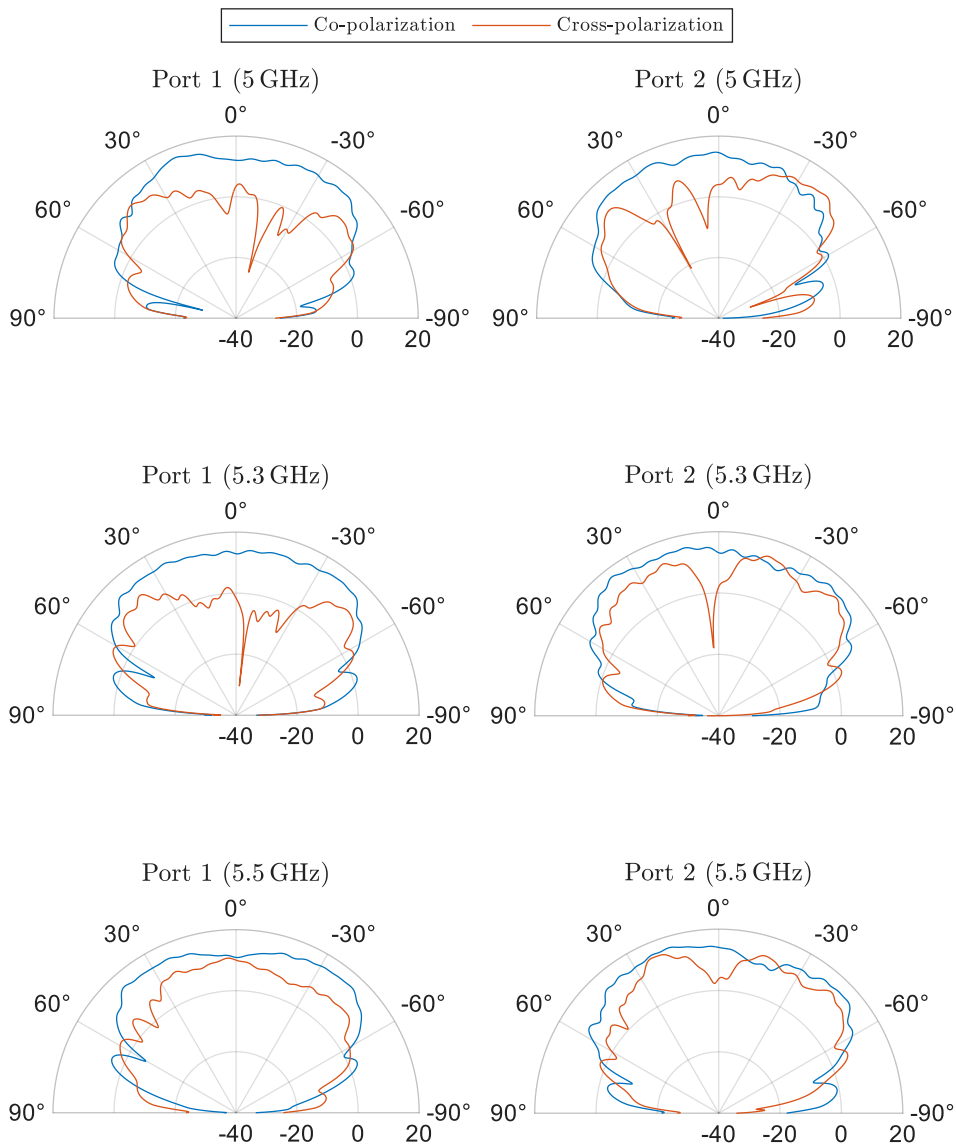


Figure B.9: Measurement 2: azimuth radiation pattern ($\varphi = 0^\circ$)

Bibliography

- [1] *CST Studio Suite*, version 2024.5, Accessed: 31 December 2024, Dassault Systèmes. [Online]. Available: <https://www.3ds.com/products-services/simulia/products/cst-studio-suite>.
- [2] *Antenna Magus*, version 2024.05, Accessed: 31 December 2024, Dassault Systèmes. [Online]. Available: <https://www.3ds.com/products-services/simulia/products/antenna-magus>.
- [3] P. Virtanen, R. Gommers, T. E. Oliphant *et al.*, “SciPy 1.0: Fundamental Algorithms for Scientific Computing in Python”, *Nature Methods*, vol. 17, pp. 261–272, 2020. DOI: [10.1038/s41592-019-0686-2](https://doi.org/10.1038/s41592-019-0686-2).
- [4] *MATLAB*, version 23.2.0 (R2023b), Accessed: 31 December 2024, The MathWorks Inc. [Online]. Available: <https://www.mathworks.com>.
- [5] C. Balanis, *Advanced Engineering Electromagnetics*. Wiley, 2012, ISBN: 9781118213483.
- [6] D. Griffiths, *Introduction to Electrodynamics*. Prentice Hall, 1999, ISBN: 9780139199608.
- [7] A. Zangwill, *Modern Electrodynamics*. Cambridge University Press, 2013, ISBN: 9780521896979.
- [8] E. Titchmarsh, *Introduction to the Theory of Fourier Integrals*. Clarendon Press, 1948, ISBN: 9780608133492.
- [9] A. Oppenheim, A. Willsky and S. Nawab, *Signals & Systems*, 2nd ed. Prentice Hall, 1997, ISBN: 9780136511755.
- [10] J. A. Ruiz-Cruz, M. M. Fahmi, M. Daneshmand and R. R. Mansour, “Compact reconfigurable waveguide circular polarizer”, in *2011 IEEE MTT-S International Microwave Symposium*, Baltimore, MD, USA, 2011, pp. 1–4. DOI: [10.1109/MWSYM.2011.5972872](https://doi.org/10.1109/MWSYM.2011.5972872).
- [11] X. Wang, X. Huang and X. Jin, “Novel square/rectangle waveguide septum polarizer”, in *2016 IEEE International Conference on Ubiquitous Wireless Broadband (ICUWB)*, Nanjing, China, 2016, pp. 1–4. DOI: [10.1109/ICUWB.2016.7790510](https://doi.org/10.1109/ICUWB.2016.7790510).
- [12] H. Song, L. Jia, J. Tan, Y. Zhang and S. Liu, “Design of Wideband Quad-Ridge Waveguide Polarizer”, in *2023 4th China International SAR Symposium (CISS)*, Xian, China, 2023, pp. 1–6. DOI: [10.1109/CISS60136.2023.10379971](https://doi.org/10.1109/CISS60136.2023.10379971).
- [13] G. Virone, R. Tascone, O. A. Peverini and R. Orta, “Optimum-Iris-Set Concept for Waveguide Polarizers”, *IEEE Microwave and Wireless Components Letters*, vol. 17, no. 3, pp. 202–204, Mar. 2007. DOI: [10.1109/LMWC.2006.890474](https://doi.org/10.1109/LMWC.2006.890474).
- [14] S. Pilnyay, A. Bulashenko, H. Kushnir and O. Bulashenko, “New Tunable Iris-Post Square Waveguide Polarizers for Satellite Information Systems”, in *2020 IEEE 2nd International Conference on Advanced Trends in Information Theory (ATIT)*, Kyiv, Ukraine, 2020, pp. 342–348. DOI: [10.1109/ATIT50783.2020.9349357](https://doi.org/10.1109/ATIT50783.2020.9349357).

- [15] B. Deutschmann and A. F. Jacob, “Broadband Septum Polarizer With Triangular Common Port”, *IEEE Transactions on Microwave Theory and Techniques*, vol. 68, no. 2, pp. 693–700, Feb. 2020. DOI: 10.1109/TMTT.2019.2951138.
- [16] H.-Y. Yu, J. Yu, X. Liu, Y. Yao and X. Chen, “A Wideband Circularly Polarized Horn Antenna With a Tapered Elliptical Waveguide Polarizer”, *IEEE Transactions on Antennas and Propagation*, vol. 67, no. 6, pp. 3695–3703, Jun. 2019. DOI: 10.1109/TAP.2019.2905789.
- [17] L. A. Rud and K. S. Shpachenko, “Polarizers on sections of square waveguides with inner corner ridges”, in *2011 VIII International Conference on Antenna Theory and Techniques*, Kyiv, Ukraine, 2011, pp. 338–340. DOI: 10.1109/ICATT.2011.6170775.
- [18] S. Bhardwaj and J. Volakis, “Hexagonal waveguides: New class of waveguides for mm-wave circulalry polarized horns”, in *2018 International Applied Computational Electromagnetics Society Symposium (ACES)*, Denver, CO, USA, 2018, pp. 1–2. DOI: 10.23919/ROPACES.2018.8364165.
- [19] S. Bhardwaj and J. L. Volakis, “Hexagonal Waveguide Based Circularly Polarized Horn Antennas for Sub-mm-Wave/Terahertz Band”, *IEEE Transactions on Antennas and Propagation*, vol. 66, no. 7, pp. 3366–3374, Jul. 2018. DOI: 10.1109/TAP.2018.2829842.
- [20] S. Bhardwaj and J. L. Volakis, “Circularly-polarized horn antennas for terahertz communication using differential-mode dispersion in hexagonal waveguides”, in *2017 IEEE International Symposium on Antennas and Propagation & USNC/URSI National Radio Science Meeting*, San Diego, CA, USA, 2017, pp. 2571–2572. DOI: 10.1109/APUSNCURSINRSM.2017.8073328.
- [21] E. Garcia-Marin, J. L. Masa-Campos, P. Sanchez-Olivares and J. A. Ruiz-Cruz, “Bow-Tie-Shaped Radiating Element for Single and Dual Circular Polarization”, *IEEE Transactions on Antennas and Propagation*, vol. 68, no. 2, pp. 754–764, Feb. 2020. DOI: 10.1109/TAP.2019.2943357.
- [22] M. Born, E. Wolf and A. Bhatia, *Principles of Optics: Electromagnetic Theory of Propagation, Interference and Diffraction of Light*. Cambridge University Press, 1999, ISBN: 9780521642224.
- [23] H.-U. Nickel, “Cross Reference for Hollow Metallic Waveguides”, SPINNER GmbH, Tech. Rep. TD-00036, Jul. 2024, Accessed: 29 December 2024. [Online]. Available: https://www.spinner-group.com/images/download/technical_documents/SPINNER_TD00036.pdf.
- [24] I. Fabregas, K. Shamsaifar and J. Rebollar, “Coaxial to rectangular waveguide transitions”, in *IEEE Antennas and Propagation Society International Symposium 1992 Digest*, Chicago, IL, USA, 1992, 2122–2125 vol.4. DOI: 10.1109/APS.1992.221447.
- [25] M. Durga, S. Tomar, S. Singh and L. Suthar, “Millimeter wave in-line coaxial-to-rectangular waveguide transition”, in *2011 IEEE Applied Electromagnetics Conference (AEMC)*, Kolkata, 2011, pp. 1–3. DOI: 10.1109/AEMC.2011.6256817.
- [26] S. K. Karki, J. Ala-Laurinaho and V. Viikari, “Dual-Polarized Probe for Planar Near-Field Measurement”, *IEEE Antennas and Wireless Propagation Letters*, vol. 22, no. 3, pp. 576–580, Mar. 2023. DOI: 10.1109/LAWP.2022.3218731.
- [27] N. A. Aboserwal, C. A. Balanis and C. R. Birtcher, “Conical Horn: Gain and Amplitude Patterns”, *IEEE Transactions on Antennas and Propagation*, vol. 61, no. 7, pp. 3427–3433, Jul. 2013. DOI: 10.1109/TAP.2013.2256453.

- [28] C. Balanis, *Antenna Theory: Analysis and Design*. Wiley, 2015, ISBN: 9781119178996.
- [29] *CST Python Libraries*, Dassault Systèmes Deutschland GmbH, Accessed: 29 December 2024. [Online]. Available: https://space.mit.edu/RADIO/CST_online/Python/main.html.